Automatic Image Segmentation and Correlation in Radiotherapy Verification

by

Hui Wang
Department of Physics
McGill University, Montreal
April, 1993

A Thesis Submitted to the Faculty of Graduate Studies and Research in Partial Fulfillment of the Requirements of the Degree of Master of Science

Abstract

Two active topics in radiation therapy treatment verification, portal image segmentation and correlation, are addressed, and a robust algorithm for automatic segmentation of portal images and portal image registration with respect to a reference image is developed. Morphological techniques have been intensively applied in all stages of the segmentation part of this algorithm, from edge detection to feature extraction. An important issue, edge enhancement, is discussed particularly in detail. The performance of the morphological edge detection technique on portal images is compared with that of local gradient operators and optimal edge detectors, while the advantage of the morphological edge detection and segmentation techniques is justified. The treatment field mask is proposed as the landmark for portal-simulator image correlation achieved by matching inertia moments of landmarks. The effect of two different landmarks, the treatment field mask and the treatment field contour, is examined with this correlation method, and the superiority of using the treatment field mask is shown.

Résumé

Deux sujets d'importance pour la vérification de traitements en radiothérapie, la segmentation et la corrélation des images portaux, sont adressés. En plus, un algorithme robuste qui segmente automatiquement des images portaux et qu enregistre une image par rapport à une image de référence est dévelopé. Des techniques morphologiques ont été appliquées intensivement à tour les niveaux de la section de segmentation dans l'algorithme, incluant la détection de bords jusqu'à l'extraction de traits. L'amélioration de bordures, un sujet d'importance, est souligné. La performance de la technique morphologique de la détection de bordures sur des images portaux est comparée à celle des opérateurs de gradients locausx et des détecteurs de bordures tout en justifiant l'avantage de la technique morphologique et celle de segmentation. Le masque du champ de traitement est utilisé comme point de repére pour la corrélation des images sijulateurs et portaux qui est accomplie en mettant ensemble les moments d'inertie des points de repère. L'effet d'utiliser le masque de champ de traitement ou le contour du champ de traitement comme point de repère pour cette méthode de corrélation est examiné, et la supériorité obtenu en utillisant le masque est démontrée.

Original Contribution

A robust algorithm is developed for automatic segmentation of double exposure portal images which is required for contrast enhancement of the portal images with the selective histogram equalization technique (SHE), and for registration of the enhanced portal image with respect to the corresponding simulator image. Based on morphological edge detection morphological feature extraction techniques, the algorithm employs a dynamic approach to search the optimal segmentation for each individual portal image and therefore can accommodate very difficult situations. A new landmark, the treatment field mask, is proposed for the registration of a portal image onto the corresponding simulator image by matching inertia moments. We find that the inertia moments of the treatment field mask are less sensitive to shape distortions than the inertia moments of the field contour, thus resulting in robust registration.

Acknowledgements

I am very grateful to my supervisor, Dr. B. Gino Fallone, who not only introduced me into this interesting field of portal imaging when I was looking for a thesis project a year ago, but also gave me full support in all aspects of this research.

I would like to thank Mr. Ian Crooks, MR physicist, for the inspiring discussions I had with him and for his technical help, especially for allowing me to use his program for image file format conversion, which have saved me a lot of time and labor. Special thanks go to the technicians of the Department of Radiation Oncology at the Montreal General Hospital for helping accumulate the portal films and simulator films used in this research. I also wish to thank my fellow students in Medical Physics for their kindness and friendship, and I would like to thank Ms. Chantal Audet for translating the abstract into French.

This project is partially supported by the Sterling Winthrop Imaging Research Institute and the Medical Research Council of Canada. The Teaching Assistantship from the Department of Physics is also gratefully acknowledged.

Contents

List of Figures

Chapter 1

Introduction

1.1 General Introduction

Portal films acquired with photons emanating from radiotherapy treatment machines are the conventional means of treatment verification. But several problems exist in this verification procedure. Portal images are of very poor quality due to the high energy of the photons emerging from treatment machines. Comparison of portal images with reference images are made even more difficult by the fact that reference images are obtained from other imaging modalities which exhibit different characteristics from portal images. Digital image processing techniques have been employed to improve the quality of portal images for better visualization, and to manipulate digital images for quantitative and automatic verification. As more and more on-line portal imagers are installed on treatment machines, postprocessing of digital portal images becomes more and more important. This thesis addresses some active topics in portal imaging, such as treatment field extraction from portal images and correlation of portal images with respect to a

reference image. A robust algorithm for automatic segmentation of portal images by using morphological techniques and portal image registration by using the treatment field as landmark is also presented.

1.2 Thesis Organization

An overview of portal imaging is given in Chapter 2 and some problems currently under investigation in portal image segmentation and treatment verification are presented at the same time.

In Chapter 3, the image processing system, especially the special image processing hardware employed in this research is described. Technical aspects such as film digitization and image format modification are also clarified.

As a preparation of Chapter 5, Chapter 4 introduces the principles of mathematical morphology and formalizes the morphological approach in image processing. Operations used in this thesis are explained and illustrated in detail.

Starting from low level processing operations, the performance of different edge detectors on portal images is compared and the advantage of morphological edge detection and segmentation techniques is justified in Chapter 5. A robust algorithm for automatic segmentation of double exposure portal images is developed, thereafter.

Image correlation by using the inertia moments of landmarks and the condition for using this method on portal simulator image pairs is discussed in Chapter 6. The advantage of using the radiation field masks as correlation landmarks over the treatment

field contour is also proven.

Finally in Chapter 7, conclusions of this research are summarized. Limitations of this image segmentation and correlation algorithm for radiation treatment verification are discussed and some future work that can improve the performance of this algorithm is proposed.

Chapter 2

Background

2.1 Portal Imaging

The successful accomplishment of a radiotherapy treatment depends on the accurate setup of the radiation beam with respect to the tumor within the patient body and the verification of patient movement during the treatment. To achieve accurate beam localization, visualization of the tumor and the surrounding anatomy is needed. The acquisition of an image on a therapy machine is called portal imaging or megavoltage imaging compared to x-ray imaging in diagnostic radiology[A1], and the image obtained is called a portal image. Ideally, an on-line imaging system that can work in real-time is needed for interactive setup of the patient and monitoring of the patient during the treatment. A large number of investigations on on-line portal imaging systems have been performed in the past decade[B5]. The systems can be categorized into three types, metal plate-fluorescent screen based systems, liquid ionization chamber systems and solid state systems. Although having been used clinically, on-line portal imaging systems are well

under development. The regular means of beam localization remains the portal film.

To obtain a double-exposure portal[A1], a radiographic film is placed on the beam exit side of the patient and is exposed twice, once with the blocked field shaped according to the prescribed field contour, another time with the open field. This results in a dark field shadow on a bright anatomy background. The double exposure technique has the advantage of showing the position of the field relative to the anatomy so that this position on the portal can be compared with that on a reference image for verification. The reference image may be a simulator film acquired during the simulation procedure performed before the treatment, or another portal image for fractionated treatment.

2.2 Processing of Digital Portal Images

In the energy range of therapy photons ($1 \sim 10$Mev), the dominant interaction between photons and the human body is Compton scattering[J2]. Different constituents of the body, like soft tissue, fat and bones, have very close mass attenuation coefficients, resulting in very low radiation contrast in a portal image[T2]. Moreover, scattering blurs the image and introduces noise. Therefore, portal images have low contrast, low spatial resolution and high noise level. Digital image processing techniques have been employed to improve the quality of portal images.

2.2.1 Contrast Enhancement

Contrast enhancement can be achieved with different kinds of histogram based transformations, among which histogram equalization is a very popular one[P1]. The histogram of an image is a plot of number of pixels versus pixel value, i.e. the occurrence of pixels at each gray level. For a low contrast image, its histogram occupies a small region of the whole display range. Gray level variation corresponding to the content of the image is small. The histogram equalization process transforms the value of each pixel such that the histogram of the transformed image is uniform across the whole display range, i.e. to assign equal number of pixels to each display level to achieve the optimum visualization. When applied to double exposure portal images, the effect of global histogram equalization is limited. On a double exposure portal film, the treatment field is a dark shadow overlaid on the background anatomy resulting in two major peaks in the histogram. The histogram can not be sufficiently stretched by a global histogram equalization because it can not be extended out of the display range. Selective histogram equalization (SHE) technique has been developed for further contrast enhancement[C2][C3][L2][C4].

Selective Histogram Equalization

In SHE, local histogram equalization is applied separately to the treatment field and the surrounding area, which is equivalent to filtering out the dark treatment field shadow and applying histogram equalization. This technique requires accurate delineation of the treatment field from the surrounding area. Segmentation is also required for contrast

enhancement of on-line portal images, which are acquired with single exposure, because the dark surrounding area will cause the same effect as the dark treatment field on a double exposure image. Applying histogram equalization to the treatment field on a single exposure image instead of to the whole image will give better visualization.

2.2.2 Segmentation of Portal Images

Different techniques for portal image segmentation have been developed. Bijhold et al[B3] used contour connecting technique to extract the treatment field border from the edge-enhanced image by the Sobel edge detector. The Sobel, like other gradient operators, is very sensitive to noise due to its small kernel size (3×3). The accuracy of the extracted field boundary is limited by the relatively high noise level of portal images.

To suppress noise sensitivity in edge detection, Leszczuski et al used one of the optimal edge detectors, the first derivative of the Gaussian (DOG), to smooth the image before edge enhancement, and incorporated a more sophisticated stage in contour connection[L2]. However, the DOG operator requires convolution with large kernels therefore is computation intensive, which is a major issue in on-line portal imaging systems. The first derivative of Gaussian is the first implementation of the ideal optimal edge detector which is characterized by the three criteria given by Canny[C1]. A better implementation of the ideal optimal edge detector has been given by Deriche and it outperforms the first derivative of Gaussian operator according the Canny criteria[D2].

Morphological techniques were applied to portal image segmentation by Crooks

et al[C4] but the edge enhancement was based on the Sobel operator and the extraction approach was based on a single predefined criterion. Although relatively crude, it showed the potential of morphological techniques in automatic segmentation of portal images. As a continuation, this thesis is aiming at increasing the robustness of automatic segmentation of portal images by using new approaches in edge enhancement and feature extraction in order to increase the degree of automation of the whole treatment verification procedure.

2.3 Treatment Verification with Portal Films

Radiotherapy treatment is planned according to the simulation carried out before the treatment. A simulator is a regular x-ray unit but with the same geometric structure as a therapy machine so that the patient can be set-up on the therapy machine according to the simulation. The radiation oncologist marks the treatment field on the simulator film. The technician makes field shaping blocks according to the prescribed field. Since most treatment machines do not have on-line portal imagers, treatments are verified by comparing a portal film with the corresponding simulator film. Although the treatment machine has the same mechanical structure with the simulator, the film to source distance and the orientation of the cassette in the image plane may be different. This results in different magnification and image orientation on the portal film and the simulator film and makes visual comparison labor intensive. When the films are digitized, the images can be easily manipulated and correlated through a geometric transformation. A significant

amount of research has been performed on matching digital portal and simulator images.

Meertens et al used landmarks manually made from anatomical structures on both portal and simulator images to match the two images and to observe the shift of the treatment field relative to the prescribed field[M3]. Balter et al used a method of correlating open curve landmarks by using their curvatures to match portal and simulator images but the landmarks have also to be drawn manually[B2]. Since the treatment field contour can be extracted automatically, Bijhold et al has investigated matching digital line drawings by using their inertia moments, aimed at automatic on-line treatment verification[B4]. This method uses the treatment field contour automatically extracted from the portal image and the prescribed field contour which is predrawn on the simulator image as landmarks and calculates the parameters needed in the geometric transformation from the inertia moments of the two digital contours. Two problems may exist in this approach, a) fluctuation on the automatically extracted treatment field contour due to noise in the portal image, b) shape distortion of treatment field due to errors in the manufacturing of the treatment field shaping blocks, which happens very frequently in daily treatment. A compact object has larger inertia moments than its contours. Therefore, we believe that using compact field masks as landmarks can be expected to give stronger resistance to fluctuation on the field border and acceptable field shape distortion.

Chapter 3

Materials and Methods

3.1 Image Processing System

An imaging system having hardware processing ability has been employed in this study. It consists of a VDC3874 video camera (Sanyo Electric Inc., Japan) with a user designed light box, a CRS laser film digitizer(Du Pont, U.S.A.), a 386 PC (MaxSys Inc. U.S.A.), a Matrox Image-Series IM-1280 imaging board set (Matrox Electronic Systems, Canada), and a Mitsubishi HL6905 Diamond Scan 19" (Mitsubishi Electric Corp., Japan) high resolution image monitor. A diagram of the system is shown in Figure 3-1.

3.1.1 Image-Series

As the central part of this system, the Image-Series performs image digitization and processing and controls image display on the image monitor. It is an intelligent board set consisted of a base board (IM -1280), a real time processor board (RTP) and a digitizer board. The three boards are connected by an image bus.

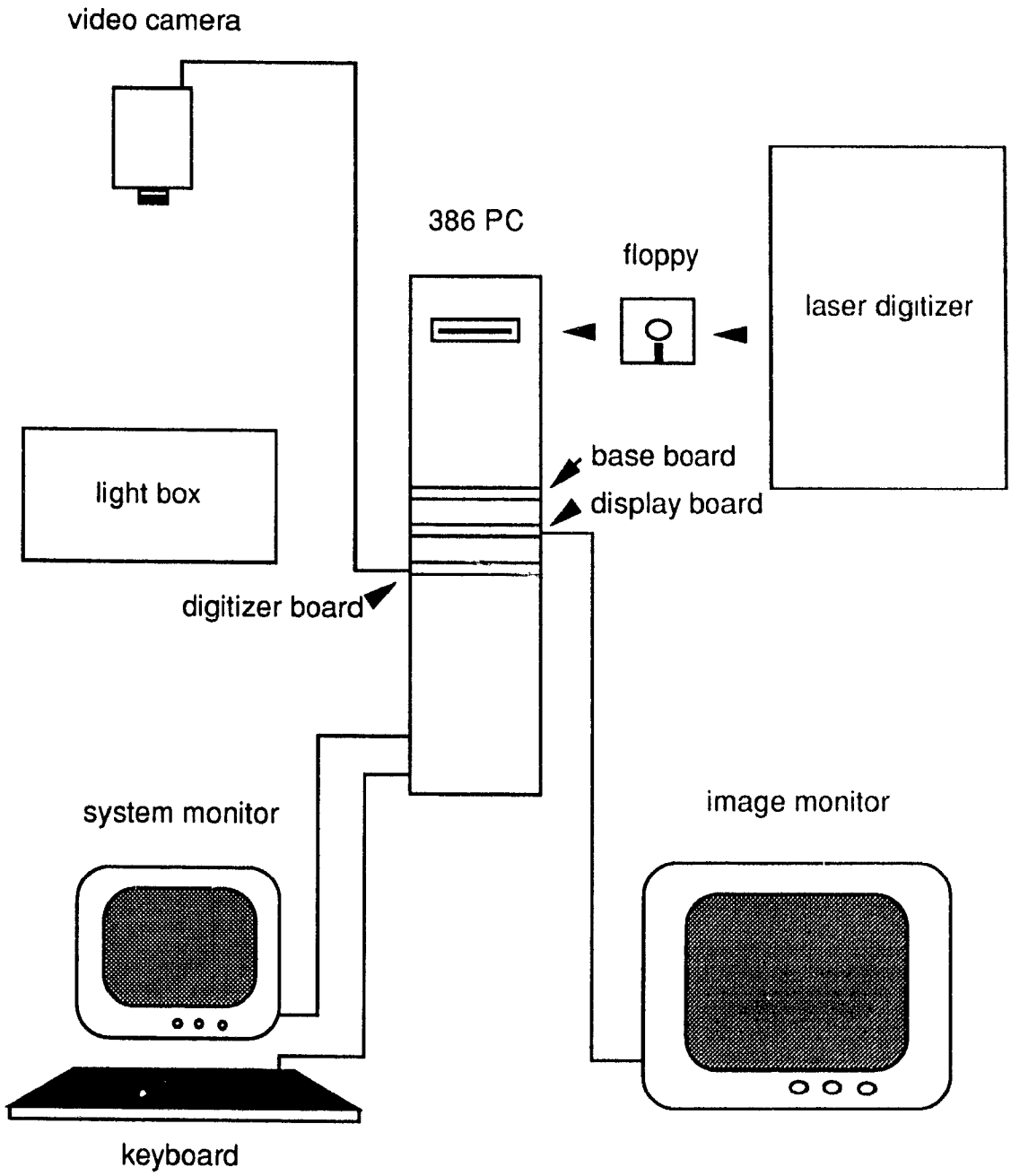

Figure 3-1: Layout of the imaging system

Base board

The Base Board is the central board of the Image-Series. It has a Graphics System Processor (GSP) which controls the whole Image Series. The GSP receives opcodes transmitted from the Host computer, decodes them, and then either sets up the appropriate hardware or executes the request itself. The base board also hosts buffers which feed data to the on-board video display controller and serve as the main storage area for images, processing and graphics. The frame buffers are organized to provide very fast data transfers between buffers and all other Image-Series boards (up to 30 million pixels per second).

Image-RTP

Consisted of a Data Formatter, a Data-Router, a Cascaded ALU, a Neighborhood Processor, a Statistical Processor, the Image-RTP makes it possible to perform several operations in one 15 MHz pass. It can perform 3×3 gray scale and 18×16 binary neighborhood operations in one pass with the Neighborhood Processor, and combine information from two sources with the Cascaded ALU. A data router allows for various data paths through the processing elements.

The Data Formatters, situated on both Image-RTP inputs, convert incoming frame buffer/digitizer data from various input types into the internal 16-bit representation used by the processing pipeline. An on-board Data Router directs data to the appropriate processing elements. It allows results from one processing element to un-

dergo further processing through other processing elements without having to store and then re-read the results. The cascaded ALU performs a variety of arithmetic and logical operations. It can pre-process the input or post -process the output of other processing elements.The neighborhood Processor can perform up to 18×16 binary and up to 63 gray scale neighborhood and morphological operations in one frame time. It supports both rectangular and hexagonal lattices in hardware. The statistical processor has an event counter/comparator, a minimum/maximum comparator, and a histogram and profile generator. This processor uses Statistical LUT as a storage area for results. The Statistical Processor can use object labels to sort the results of basic feature extraction.

Digitizer Board

The image-ASD supports both analog and digital input, accepts a wide range of source frequencies, has a programmable synchronization generator, and can accept trigger pulses for mono-shot cameras. It supports black and white video sources. or video sources with switchable filters or RGB input on three different channels. This digitizer can only send one analog color component at a time to the Image-Bus. An on-board Digitizer LUT maps digitized data.

Image-Bus

The Image Bus serves as a 30 MHz communication link between the base board and the other Image-Series boards. It is a wide dual-bus interface consisting of an I/O bus for system control, and a processing bus with two 32-bit data paths for high-speed image

processing data transfers. The two processing data paths provide simultaneous data flow both to and from data storage.

3.1.2 Host and I/O

The MaxSys 386 PC hosts the Image Series. To a large extent, it is only used as a controller. The VDC 3874 video camera has $\frac{2}{3}$" CCD array of 800×490 elements. It uses a 25mm lens to focus the image on the CCD. Video output of the camera are sent to the Image-Series and digitized by the digitizer board. Films are also digitized with the laser film digitizer which digitize a film into 844×1021 pixels with a depth of 14 bits or 1688×2042 pixels with a depth 12 bits. Digital images are displayed on the image monitor which has a resolution of 1280×1024 pixels.

3.1.3 Software

The Image-Series comes with a complete set of control, processing and graphics modules. It also has a command interpreter that allow the user to issue commands directly to the hardware, but this is performed on a very low level and is difficult to use. Noesis Visilog[N1] image processing software has been used as the user-board interface. Visilog is an image processing and analysis software package working with industry-standard Graphics User Interface. It can automatically make use of the abilities of special imaging hardwares. The PC version is developed in the MS-Windows 3.0 or higher environment, therefore, is particularly suitable for investigations for algorithm development. It also

has a library of image analysis, processing and graphics functions for user application development.

3.2 Image Acquisition

Portal and simulator image pairs are selected randomly from the patient files in Radiation Oncology in the Montreal General Hospital and the Jewish General Hospital. Simulator films are obtained from an AECL Therasim-750 simulator, and portal films are obtained from the following therapy machines: Theratron-780 Co-60 unit (Atomic Energy of Canada), Therapi-4 4MV (SHM Nuclear Systems), EMI-6 6MV (EMI Therapy Systems) and Clinac-18 10MV (Varian Associates) linear accelerators. The films cover a variety of treatment sites. Since portal films have low spatial resolution and low contrast, they are digitized with the video camera into 256×240 pixels, each pixel with a depth of 8 bits. Films are also digitized with the laser digitizer, and the image file is presently imported into the host of the imaging system via a floppy disk. The standard resolution mode ($844 \times 1021 \times 14$ bits) has been used. Since the image format of Visilog is that the depth of a pixels must be a multiple of a byte, images acquired with the laser digitizer are shrunk into 8 bits deep. An improvement may be achieved by taking advantage of the full 14 bit image, but the advantages may be marginal due to the inherently low contrast features of portal images, therefore we used the video camera for digitization most of the time.

3.3 Algorithm Implementation

Our algorithm is written in 'C' and is implemented in the standalone mode. A double exposure portal image is segmented into two sub-images by use of an automatic technique, one corresponding to the treatment field, the other corresponding to the surrounding area. The two sub-images are enhanced with histogram equalization and are combined afterwards. The extracted field mask is also kept in memory for correlation.

The simulator image is of diagnostic quality and represents the reference image. The landmark on the simulator image used for correlation with the portal is preselected with our software. The landmark is drawn directly on the simulator image with a mouse by following the prescribed field contour specified by the radiation oncologist and the resultant landmark mask is saved in a file as an image. The geometric relationship between the portal and simulator image is calculated from the inertia moments of the two landmarks and the enhanced portal is correlated to the simulator image.

Chapter 4

Mathematical Morphology

4.1 Euclidean Morphology

Morphology as a methodology in image processing was introduced by G. Matheron in the 1970s[M2]. Based on set theory, morphology deals with geometric structures inherent to an image[S1][H1][S2][D3][G1]. Geometric information in an image is analyzed by fitting some predefined small geometric shapes, called structuring element, into the image. As a probe, the structuring element is passed over the domain of an image while a set operation is applied around the neighborhood of each element of the image. The geometric information which is extracted depends on the operation applied when the structuring element is passed over the image. Since most of the morphological operations used in this study are applied on binary images, we will commence our discussion of morphology in the Euclidean plane. Two-valued images can be considered as sets of points in the Euclidean plane.

4.1.1 Fundamental Operations

Mathematical morphology is based on set theory. Morphological operations are built upon set operations which are primitive to the morphology level. Besides the usual set operations, union and intersection, another primitive operation, *translation*, has to be introduced in order to define the basic morphological operations. For a set of points A in the Euclidean plane R^2, the *translation* of A by a point x in R^2 is given by

$$A + x = \{a + x : a \in A\} \tag{4.1}$$

Now we can defined the two fundamental operations in morphology, *Minkowski addition* and *subtraction*. Given two sets A and B in the Euclidean plane R^2, the *Minkowski addition* (represented by $\oplus$) of A and B is the union of all the translates of A by each element of B,

$$A \oplus B = \bigcup_{b \in B} (A + b) \tag{4.2}$$

while the *Minkowski subtraction* (represented by $\ominus$) is the intersection of all the translates of A by each element of B,

$$A \ominus B = \bigcap_{b \in B} (A + b) \tag{4.3}$$

where b is an arbitrary element of B.

Traditionally, morphology was developed in a graphical way. Basically, a small probe is applied to every element of an image, and the manner in which this probe

fits within the image is investigated. Based on this strategy, two basic morphological operations can be defined from Minkowski addition and Minkowski subtraction. It can be proven that the Minkowski addition, $A \oplus B$, is equivalent to the union of all the translates of B by each element of A:

$$\begin{aligned} A \oplus B &= \bigcup_{y \in B} (A + y) \\ &= \bigcup_{y \in B} \left(\left[\bigcup_{x \in A} \{x\} \right] + y \right) \\ &= \bigcup_{y \in B} \bigcup_{x \in A} \{x + y\} \\ &= \bigcup_{x \in A} \left(\left[\bigcup_{y \in B} \{y\} \right] + y \right) \\ &= \bigcup_{x \in A} (B + x) \end{aligned} \tag{4.4}$$

The *dilation* of A by B is defined as

$$\mathcal{D}(A, B) = A \oplus B \tag{4.5}$$

where B is called *structuring element.*

Minkowski subtraction can be written as

$$\begin{aligned} A \ominus B &= \bigcap_{y \in B} (A + y) \\ &= \bigcap_{y \in B} \{x : x \in (A + y)\} \\ &= \bigcap_{y \in B} \{x : -y + x \in A\} \\ &= \{x : -B + x \subset a\} \end{aligned} \tag{4.6}$$

where $-B$ is defined as $-B = \{-b : b \in B\}$. This is equivalent to rotating B by 180°

about the origin, and finding the set of points by which the translation of the rotated B can fit into A.

The *erosion* operation of A by B is defined as

$$\mathcal{E}(A, B) = A \ominus (-B) \tag{4.7}$$

where B is also called structuring element. The procedures of dilation and erosion are illustrated in Figure 4-1. Three objects are shown in Figure 4-1 (a). Erosion and dilation of these objects by a small square structuring element in Figure 4-1 (b) are shown in Figure 4-1 (c) and (d), respectively. The dilation and erosion of an object by a structuring element can be seen by sliding the structuring element along the border of the object, and the outer contour drawn by the structuring element defines the dilated object while the inner contour drawn by the structuring element defines the eroded object. In Figure 4-1 (c), eroded objects are represented by the solid objects and their originals are represented by the outer contours. Symbolically, erosion is like "peeling" the objects at a depth which is half the size of the structuring element, from the outer and inner "surfaces". After erosion, the small object at the upper left corner disappears, the thin junction on the largest objects is broken, and holes on this object becomes larger. The opposite situation is shown in Figure 4-1 (d), where solid objects represent the original objects and the outer contours represent the dilated ones. Dilation is like "pasting" an object with a "coating" whose thickness is half the size of the structuring element, on the outer and inner "surfaces". After dilation, the two objects at the center are united,

the two small holes disappear while the largest one becomes smaller, and the crack on the largest object converges.

4.1.2 Complex Operations and Algorithms

Complex operations and algorithms can be built upon the two basic operations, erosion and dilation. Some complex operations and algorithms have become standard processes in morphological image processing. In our context, we will only discuss the two most common complex operations, *opening* and *closing*, and two standard algorithms, *reconstruction* and *hole-filling*, that we have used in the segmentation of portal images. The *opening* of A by B is an erosion followed by a dilation,

$$\mathcal{O}(A, B) = \mathcal{D}[\mathcal{E}(A, B), B] \tag{4.8}$$

and the *closing* of A by B is a dilation followed by an erosion,

$$\mathcal{C}(A, B) = \mathcal{E}[\mathcal{D}(A, -B), -B] \tag{4.9}$$

Opening and closing are graphically illustrated in Figure 4-2. Original objects in (a) are opened and closed with the small square structuring element in (b), and the resultant opened and closed objects are shown in (c) and (d), respectively. It can be seen in (c) that opening eliminates the two small objects and breaks the weak junction at the center of the largest object. Sharp tips are also smoothed out. On the other hand, in (d),

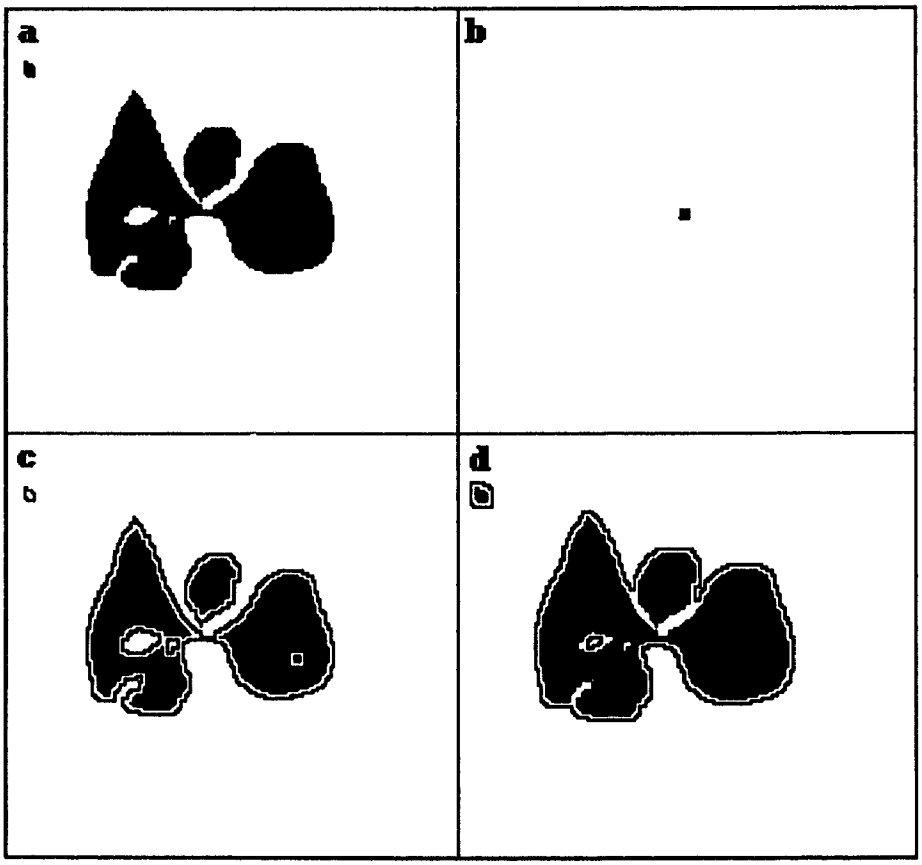

Figure 4-1: (a) original image, (b) structuring element, (c)solid objects are the eroded objects, the outer contour represents the original objects, (d) solid objects are the originals, the outer contour represents the dilated objects.

the crack and the two small holes are filled. Opening behaves similarly as erosion except it maintains the original size of an object. The same type of behavior exists between closing and dilation.

Before we proceed to reconstruction and to hole-filling, a special type of erosion and dilation must be introduced, i.e. geodesic erosion and geodesic dilation. A structuring element is called a fundamental structuring element if its size is smaller than the shortest distance between any two objects. If the fundamental structuring element is used, an erosion is called a geodesic erosion and a dilation is called a geodesic dilation.

Reconstruction picks up certain objects from an image with the use of a marker image. After reconstruction, only objects that contain a marker will remain. Suppose A is the original image, B is the marker image and e is a fundamental structuring element, the reconstruction of A with B is an iterative process of the intersection of the geodesically dilated marker image with the original image, that is represented in the following manner

$$C_{i+1} = A \cap \mathcal{D}(C_i, e)$$

where

$$C_0 = A \cap \mathcal{D}(B, e)$$

until the marker fills the whole domain of the object (convergence), i.e. $C_{i+1} = C_i$. It should be emphasized that the dilation operation involved in the reconstruction operation

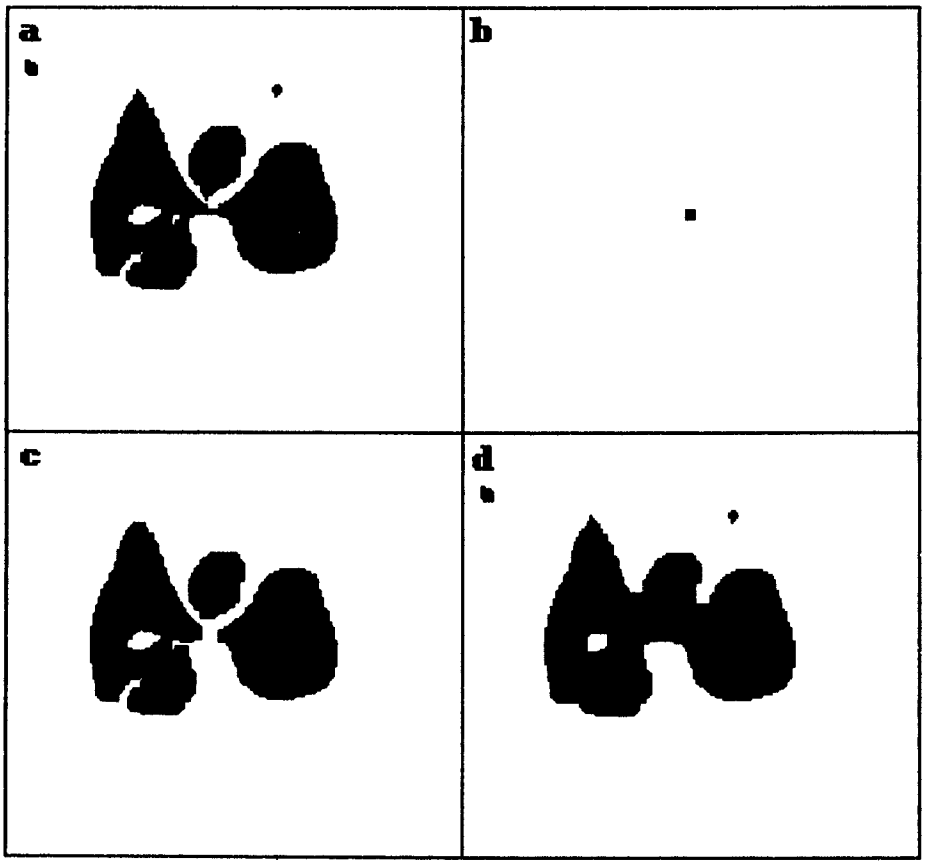

Figure 1-2: (a) original image, (b) structuring element, (c) opening of the original image, (d) closing of the original image.

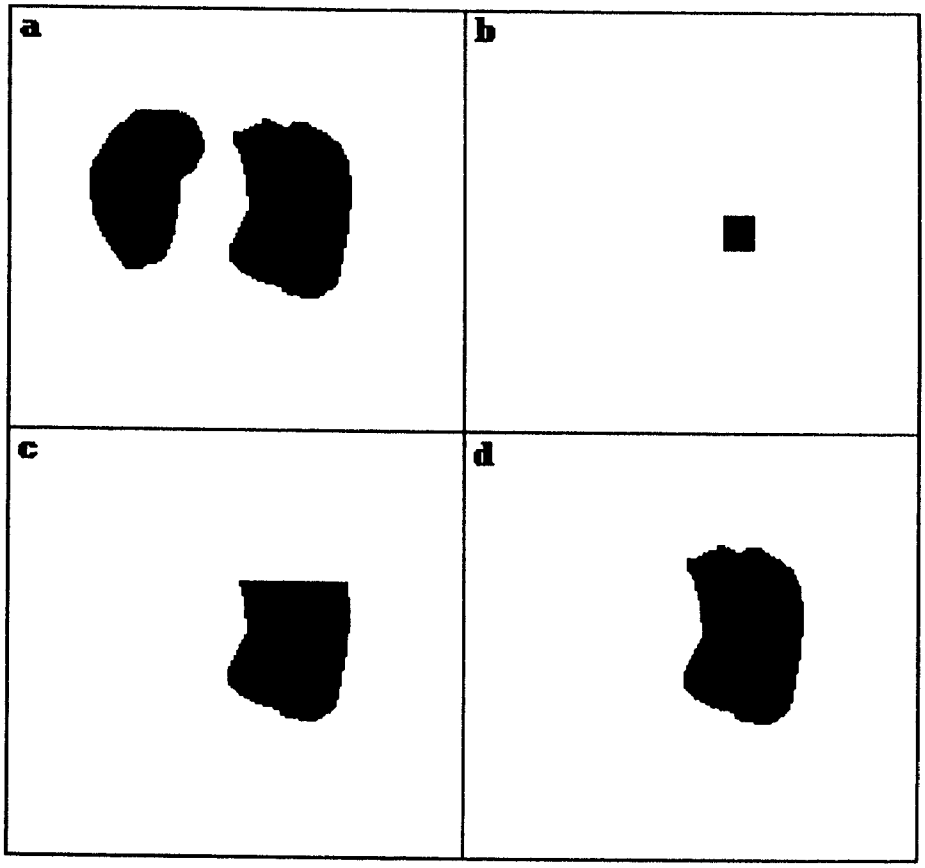

Figure 4-3: Illustration of the reconstruction procedure. (a) original image, (b) marker image, (c) intersection of the dilated marker with the original image after several iterations, (d) the reconstructed object.

must be geodesic, i.e the fundamental structuring element must be used. Otherwise, the dilated marker may "hit" another object before it is intersected with the original image. An illustration of the reconstruction operation is shown in Figure 4-3. The right object in (a) covers the marker in (b). The intersection of (a) and (b) is still the marker, the small square in (b). After dilation, the square is enlarged and it is intersected with (a) again so that it not exceed the border of the object we want to extract. This process continues until the dilated marker "flushes" all over the domain of the object we wish to extract. An intermediate step is shown in (c) and the result is shown in (d).

Hole-filling is an operation that fills the holes within objects of an image. Given an image A, and B is the boundary of the Euclidean plane, hole-filling of A is an iteration,

$$C_{i+1} = \overline{A} \cap \mathcal{D}(C_i, e)$$

where $C_0 = B$ and $\overline{A}$ is the complement of A. This process will be repeated until convergence, i.e., the next iteration does not make any difference. For example, after the nth iteration, $C_{n+1} = C_n$. The complement of C_{n+1}, $\bar{C}_{n+1}$, is then taken. As is the case with reconstruction, the dilation used in hole-filling must also be geodesic. Figure 4-4 shows the procedure of the hole-filling algorithm. To fill the hole on the right object in (a), the image is inverted to its complement (b). The image border in (c) is dilated and intersected with (b). The process, an intermediate step of which is shown in (d), continues until the background in (a) is flushed as in (e). When (e) is inverted to its complement (f), the hole on the right object has been filled.

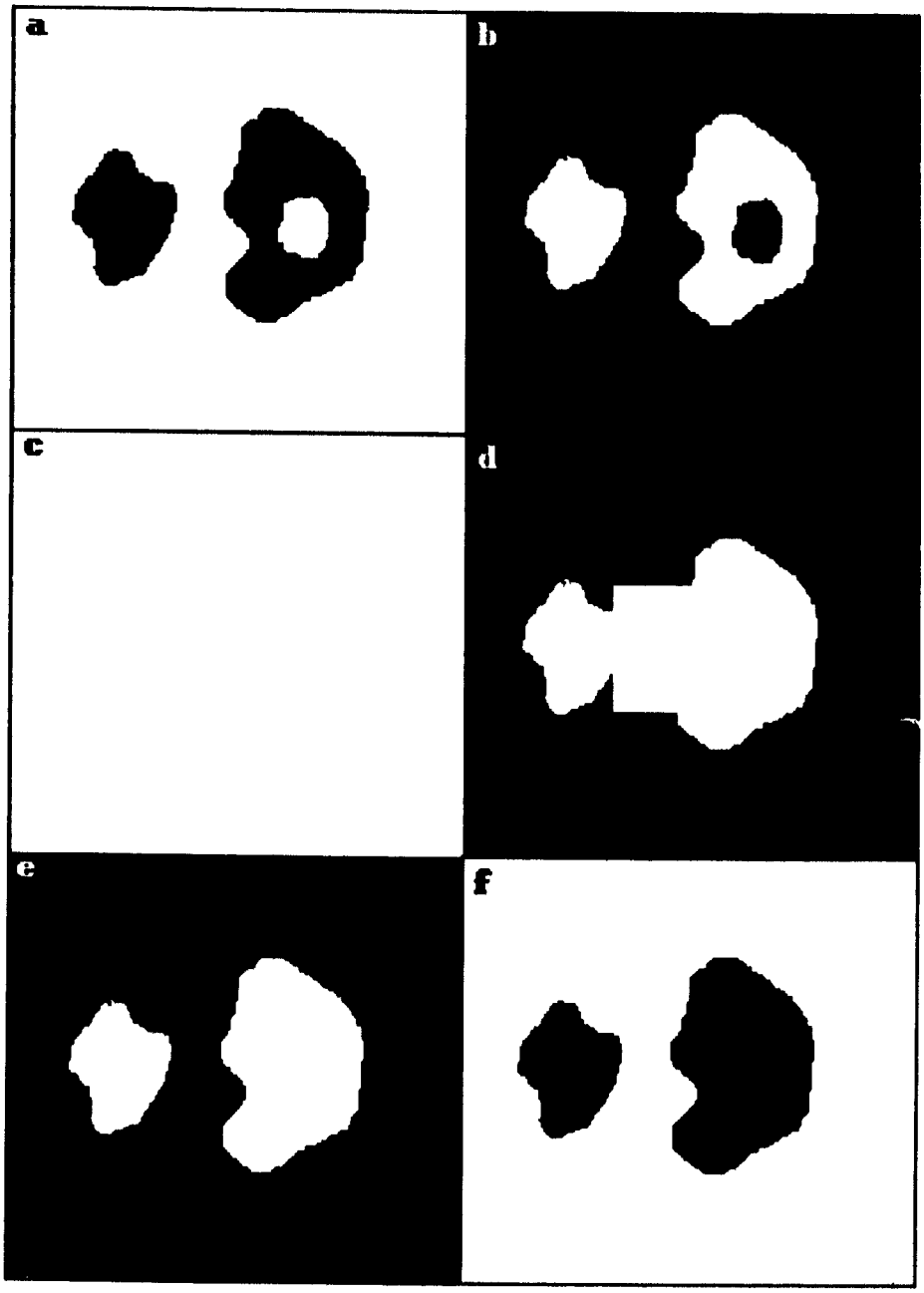

Figure 4-4: Illustration of the hole-filling operation. (a) original image, (b) complement of the original image, (c) image containing a rectanglar frame on the image border, (d) intersection of (b) with (c) after some interations, (e) the convergence of the iterations, (f) complement of (e) representing completion of the hole-filling operation.

4.2 Digital Morphology

Mathematical morphology can be easily extend from the Euclidean space to the digital situation with some modification of the definition of the basic operations. When sets in the Euclidean plane are digitized into sets of pixels, two-valued Euclidean morphology becomes binary morphology.

4.2.1 Binary Morphology

In binary morphology, digital binary images are considered sets of pixels. There are 3 possible values for a pixel, 0, 1, and $*$ (undefined). A typical image $f(i,j)$ will be represented as:

$$f = \begin{pmatrix} * & * & * & 1 & 1 & 1 & 1 & * \\ * & * & 1 & * & 1 & 1 & 1 & * \\ 1 & * & 1 & 1 & 1 & 1 & * & * \\ * & * & * & 1 & 1 & 1 & * & 1 \\ * & 1 & * & 1 & * & 1 & * & * \\ * & * & 1 & * & * & 1 & * & 1 \\ * & * & * & * & * & * & 1 & * \\ * & * & * & * & 1 & * & * & * \end{pmatrix}_{3,10} \tag{4.10}$$

where i and j are the column number and row number of a pixel respectively, and (i,j) does not necessarily have to start from $(1,1)$. For example, in Eq. (4.10) the subscript

"3, 10" implies that this matrix starts from column 3 and row 10.

Translation of f rightwards by u and downwards by v is given by

$$[\mathrm{TRAN}(f;i,j)](u,v) = f(u-i, v-j) \tag{4.11}$$

Rotation of f by 90° is given by

$$[\mathrm{NINETY}(f)](i,j) = f(j,-i) \tag{4.12}$$

Digital union of a series of images $f_k, k = 1,2,3,\cdots\cdots$, is represented as

$$[\bigvee_k f_k](i,j) = \begin{cases} 1, \text{ if there exists at least one } k' \text{ for which } f_{k'}(i,j) = 1 \\ *, \text{ if } f_k(i,j) = * \text{ for all } k \end{cases} \tag{4.13}$$

while digital intersection is represented as

$$[\bigwedge_k f_k](i,j) = \begin{cases} 1, \text{ if } f_k(i,j) = * \text{ for all } k \\ *, \text{ if there exists at least one } k' \text{ for which } f_{k'}(i,j) = * \end{cases} \tag{4.14}$$

With these primitive operations defined, we can now introduce the digital Minkowski addition,

$$F \oplus E = \bigvee_{(i,j)\in D_s} \mathrm{TRAN}(E; i, j) \tag{4.15}$$

and digital Minkowski subtraction

$$F \ominus E = \bigwedge_{(i,j)\in \mathrm{DOMAIN}(E)} \mathrm{TRAN}(E; i, j) \tag{4.16}$$

As in the continuous situation, dilation is the Minkowski addition

$$\mathrm{DILATE}(F, E) = F \oplus E = \bigvee_{(i,j)\in D_s} \mathrm{TRAN}(E; i, j) \tag{4.17}$$

and erosion is

$$\begin{aligned} \mathrm{ERODE}(F, E) &= \bigwedge_{(i,j)\in \mathrm{DOMAIN}(E)} \mathrm{TRAN}(E; -i, -j) \\ &= \bigwedge_{(i,j)\in \mathrm{DOMAIN}[\mathrm{NINETY}^2(E)]} \mathrm{TRAN}(E; i, j) \end{aligned} \tag{4.18}$$

where $\mathrm{DOMAIN}(E)$ means the domain of the structuring element E and $\mathrm{NINETY}^2(E)$ means "rotate E by 90^0 twice".

4.2.2 Gray Scale Morphology

The principles of mathematical morphology are not limited to 2-dimensional Euclidean or digital spaces. In fact, mathematical morphology was originally developed in Euclidean n-space. The difference between gray scale morphology and binary morphology is that the primitive operation applied at each pixel is different as the structuring element is

translated across the image. In gray scale morphology, the following two operations, *extended maximum* and *minimum*, represented as EXTMAX and MIN respectively, replace the union and intersection operations used in Eq. (4-2) and Eq. (4-3), respectively,

$$[\text{EXTMAX}(f,g)](i,j) = \begin{cases} \max[f(i,j),g(i,j)], \text{ if both } f \text{ and } g \text{ are defined at } (i,j) \\ f(i,j), \text{ if } f(i,j) \neq * \text{ and } g(i,j) = * \\ g(i,j), \text{ if } g(i,j) \neq * \text{ and } f(i,j) = * \\ *, \text{ if } f(i,j) = g(i,j) = * \end{cases} \tag{4.19}$$

$$[\text{MIN}(f,g)](i,j) = \begin{cases} \min[f(i,j),g(i,j)], \text{ if both } f \text{ and } g \text{ are defined at } (i,j) \\ *, \text{ if either } f \text{ or } g \text{ is not defined at } (i,j) \end{cases} \tag{4.20}$$

Dilation and erosion of an image f by a structuring element e can be expressed pixelwise

$$\mathcal{D}(f,e)_{x,y} = \max_{i,j} [f(x-i,y-j) + e(i,j)] \tag{4.21}$$

$$\mathcal{E}(f,e)_{x,y} = \min_{i,j} [a(x-i,y-j) - b(-i,-j)] \tag{4.22}$$

where (x,y) is the index of an arbitrary pixel of f and (i,j) is the index of an arbitrary

element of the structuring element kernel. The index of central element of the structuring element kernel is defined as $(0,0)$.

Morphological Gradient

A very useful gray scale morphological operation is the morphological gradient which can be used as an edge detector. Given an image f and a structuring element e, the morphological gradient of f is the subtraction of the erosion of f from the dilation of f

$$\mathcal{G}(f,e) = \mathcal{D}(f,e) - \mathcal{E}(f,e) \tag{4.23}$$

The edge response can be adjusted by changing the size and shape of the structuring element. The commonly used structuring element is

$$\begin{pmatrix} 1 & 1 & 1 \\ 1 & 1 & 1 \\ 1 & 1 & 1 \end{pmatrix}$$

which is based on the eight-connected neighbors of around a pixel. The morphological gradient is illustrated with the following example. Given an image

$$f = \begin{pmatrix} 0 & 0 & 0 & 0 & 0 & 0 & 0 \\ 0 & 8 & 8 & 8 & 8 & 8 & 0 \\ 0 & 8 & 8 & 8 & 8 & 8 & 0 \\ 0 & 8 & 8 & 8 & 8 & 8 & 0 \\ 0 & 8 & 8 & 8 & 8 & 8 & 0 \\ 0 & 8 & 8 & 8 & 8 & 8 & 0 \\ 0 & 0 & 0 & 0 & 0 & 0 & 0 \end{pmatrix}_{1,1} \tag{4.24}$$

such that dilation and erosion are represented as

$$\mathcal{D}(f, e) = \begin{pmatrix} 9 & 9 & 9 & 9 & 9 & 9 & 9 \\ 9 & 9 & 9 & 9 & 9 & 9 & 9 \\ 9 & 9 & 9 & 9 & 9 & 9 & 9 \\ 9 & 9 & 9 & 9 & 9 & 9 & 9 \\ 9 & 9 & 9 & 9 & 9 & 9 & 9 \\ 9 & 9 & 9 & 9 & 9 & 9 & 9 \\ 9 & 9 & 9 & 9 & 9 & 9 & 9 \end{pmatrix}_{1,1} \tag{4.25}$$

$$\mathcal{E}(f,e) = \begin{pmatrix} 0 & 0 & 0 & 0 & 0 & 0 & 0 \\ 0 & 0 & 0 & 0 & 0 & 0 & 0 \\ 0 & 0 & 9 & 9 & 9 & 0 & 0 \\ 0 & 0 & 9 & 9 & 9 & 0 & 0 \\ 0 & 0 & 9 & 9 & 9 & 0 & 0 \\ 0 & 0 & 0 & 0 & 0 & 0 & 0 \\ 0 & 0 & 0 & 0 & 0 & 0 & 0 \end{pmatrix}_{1,1} \tag{4.26}$$

the morphological gradient is given by

$$\mathcal{G}(f,e) = \begin{pmatrix} 9 & 9 & 9 & 9 & 9 & 9 & 9 \\ 9 & 9 & 9 & 9 & 9 & 9 & 9 \\ 9 & 9 & 0 & 0 & 0 & 9 & 9 \\ 9 & 9 & 0 & 0 & 0 & 9 & 9 \\ 9 & 9 & 0 & 0 & 0 & 9 & 9 \\ 9 & 9 & 9 & 9 & 9 & 9 & 9 \\ 9 & 9 & 9 & 9 & 9 & 9 & 9 \end{pmatrix}_{1,1} \tag{4.27}$$

What remains in G is simply the representation of the edge of f.

4.2.3 Iterative Property

A very important property of mathematical morphology is that, when uniform structuring element is used, large size erosion and dilation can be implemented as iterations of erosion

and dilation with a small structuring element, respectively. For example, dilation with the 3×3 kernel

$$\begin{pmatrix} 1 & 1 & 1 \\ 1 & 1 & 1 \\ 1 & 1 & 1 \end{pmatrix}$$

applied twice is equivalent to single dilation with the 5×5 kernel

$$\begin{pmatrix} 1 & 1 & 1 & 1 & 1 \\ 1 & 1 & 1 & 1 & 1 \\ 1 & 1 & 1 & 1 & 1 \\ 1 & 1 & 1 & 1 & 1 \\ 1 & 1 & 1 & 1 & 1 \end{pmatrix}$$

because the 8-connected neighbors of the 3×3 kernel are the elements on the border of the 5×5 kernel, and the operation applied around the neighborhood of any pixel of an image is comparison. Since the number of calculations is proportional to the square of the size of the structuring element, the iterative method can significantly shorten calculation time. For an $n \times n$ image, in which the border effect is ignored, dilation with the 3×3 kernel requires $(9-1) \cdot n^2$ comparisons while dilation with the 5×5 kernel requires $(25-1) \cdot n^2$ comparisons. Therefore, the iteration method is approximately $[(25-1) \cdot n^2]/[2 \cdot (9-1) \cdot n^2] = 1.5$ times faster than the direct method. Since calculation time is a major issue in portal image processing, all the morphological operations we used in this project are performed iteratively by using the 3×3 constant structuring element.

With the basic concepts and operations of mathematical morphology introduced, we can now proceed to the next chapter where we discuss how these operations are employed to build a robust algorithm for the extraction the radiation field from double exposure portal images.

Chapter 5

Portal Image Segmentation

5.1 Basic Approach

There are two approaches in image segmentation, region oriented and edge oriented[B1]. The region oriented approach classifies pixels into different categories according to some properties of the pixels and sorts them into different regions. In the edge oriented approach, different regions are differentiated by their boundaries. The region oriented approach is not appropriate for the segmentation of double exposure portal images because it is difficult to find any measure except gray level that is very different inside the treatment field from that which is outside the treatment field. Moreover, even the gray value is not uniform inside the treatment field since the treatment field is only a transparent shadow on the anatomy. An additional difficulty is that the position of the treatment field relative to the anatomy is specified by the field boundary requiring that the field boundary must be accurately localized. Because of these reasons, edge oriented approach is the natural choice in portal image segmentation.

5.2 Edge Detection

5.2.1 Gradient Operators

An edge in a gray scale image is defined as a discontinuity in gray value. As a discontinuity in a two variable function $f(x, y)$ can be accentuated by its gradients $\frac{\partial f}{\partial x}$ and $\frac{\partial f}{\partial y}$, an edge operator for a gray scale image $I(i, j)$ can be designed as

$$\triangle_1(i,j) = I(i,j+1) - I(i,j) \tag{5.1}$$

along the horizontal direction and

$$\triangle_2(i,j) = I(i+1,j) - I(i,j)$$

along the vertical direction. These edge detectors are called Roberts Gradient Edge Detectors[R1]. Edge detection is implemented by convolution with the following kernels,

$$\begin{bmatrix} 0 & 0 & 0 \\ 0 & -1 & 1 \\ 0 & 0 & 0 \end{bmatrix}, \begin{bmatrix} 0 & 0 & 0 \\ 0 & -1 & 0 \\ 0 & 1 & 0 \end{bmatrix}$$

which enhance edges in the horizontal and vertical directions, respectively. The magnitude G and orientation Θ of the gradient are defined as,

$$G(i,j) = \sqrt{[\triangle_1(i,j)]^2 + [\triangle_2(i,j)]^2} \tag{5.2}$$

$$\Theta(i,j) = \arctan\left(\frac{\triangle_2(i,j)}{\triangle_1(i,j)}\right) \tag{5.3}$$

The Roberts edge detectors are sensitive to noise since only the difference with one immediate neighbor is considered. Larger kernels have been designed to overcome the sensitivity to noise, such as the Prewitt[P2] and Sobel[D1] edge detectors, shown below for the horizontal and vertical direction, respectively:

$$\text{Prewitt} \quad \begin{bmatrix} 1 & 1 & 1 \\ 0 & 0 & 0 \\ -1 & -1 & -1 \end{bmatrix}, \begin{bmatrix} -1 & 0 & 1 \\ -1 & 0 & 1 \\ -1 & 0 & 1 \end{bmatrix}$$

$$\text{Sobel} \quad \begin{bmatrix} 1 & 2 & 1 \\ 0 & 0 & 0 \\ -1 & -2 & -1 \end{bmatrix}, \begin{bmatrix} -1 & 0 & 1 \\ -2 & 0 & 2 \\ -1 & 0 & 1 \end{bmatrix}$$

After edge enhancement, the gradient image is usually thresholded to eliminate noise. Some edge detectors, such as the Laplacian operator, can also be based on the second order derivatives. For a two variable function $f(x,y)$, its Laplacian is

$$\nabla^2(x,y) = \frac{\partial^2 f(x,y)}{\partial x^2} + \frac{\partial^2 f(x,y)}{\partial y^2} \tag{5.4}$$

The 4-neighbor Laplacian edge detector is designed as

$$L(i,j) = I(i-1,j) + I(i,+1,j) + I(i,j-1) + I(i,j+1) - 4I(i,j) \qquad (5.5)$$

and can be implemented as convolution with the Laplacian kernel,

$$\begin{bmatrix} 0 & 1 & 0 \\ 1 & -4 & 1 \\ 0 & 1 & 0 \end{bmatrix}$$

Instead of a local maxima, the response of the Laplacian operator to an edge is a pair of peaks, one positive and the other negative. The zero-crossing point corresponds to the position of the edge.

5.2.2 Optimal Edge Detectors

Gradient operators and Laplacian operators are very sensitive to noise because only a very small neighborhood around a pixel is considered. Based on the assumption that local variations corresponding to edge transitions are slower than those corresponding to noise, optimal edge detectors have been designed to suppress noise at the same time as to obtain good edge localization by smoothing the image with some filter before taking the gradient[M1]. For simplicity, let us consider a one dimension signal $f(x)$ and smooth

it with a filter $h(x)$,

$$g(x) = f(x) * h(x) = \int_{-\infty}^{+\infty} f(x-t)h(t)dt \tag{5.6}$$

and the gradient of the smoothed signal is

$$g'(x) = \int_{-\infty}^{+\infty} f'(x-t)h(t)dt \tag{5.7}$$

If the filter has a finite range $[-a, a]$, $g'(x)$ can, by integration by parts, be reduced to

$$g'(x) = \int_{-a}^{a} f(x-t)h'(t)dt \tag{5.8}$$

Thus, edge detection is equivalent to convolving the image with the first derivative of a filter. The optimal edge detector is characterized by the following three criteria[C1]: a) The probability of failing to detect real edges and falsely responding to nonedge fluctuation should be small. Since probability of success depends on signal to noise ratio, this criterion corresponds to the maximization of the signal-to-noise ratio. b) The location of the edge points accentuated by the operator should be as close as possible to the center of true edge. c) Only one response to a single edge should exist. There are different ways to characterize these criteria mathematically, therefore the implementation of the optimal edge detector is not unique. But the performance of different implementation can be evaluated by these criteria.

One approximation to the optimal edge detector is the first derivative of the Gaussian (DOG)[M1],

$$\frac{dh(x)}{dx} = -\frac{x}{\sigma^2}\exp\left(-\frac{x^2}{2\sigma^2}\right) \tag{5.9}$$

where σ is the standard deviation of the Gaussian function. A unique feature of portal images is that the field edge has bigger penumbra than anatomy edges since the collimators are closer to the focal spot than is the patient, resulting in a wide slope in the gray value across the field border. This feature can be used to differentiate field edge from anatomy edges. The DOG operator has been used by Leszczynski et al to segment portal images acquired from an on-line imager[L2]. While the DOG operator can accentuate broad edges and depress sharp ones, it requires convolution with a large kernel. For a 256×256 portal image, the standard deviation σ of the Gaussian function has been shown to be $2 \sim 3$ which corresponds to a kernel size of approximately 11. To accelerate the process of edge detection, we investigated the performance of two types of edge detectors on double exposure portal images, the Canny-Deriche and the morphological gradient, .

The Canny-Deriche operator is a better implementation of the optimal edge detector. It gives better performance than the DOG operator according to the three criteria of the optimal edge detector[D2], and was implemented in a highly recursive fashion. This filter is described by,

$$h(x) = (1 + \alpha|x|)e^{-\alpha|x|}. \tag{5.10}$$

and the detector is given by

$$\frac{dh(x)}{dx} = -\alpha^2 x e^{-\alpha|x|} \tag{5.11}$$

Optimization between noise suppressing and good edge localization can be achieved by adjusting the spreading coefficient α. The smaller the spreading coefficient is, the stronger the smoothing effect is. For double exposure portal images, we found that the best α is around 0.5. Since the Canny-Deriche edge detector is implemented recursively, the calculation time is independent of the value of α.

5.2.3 Morphological Edge Detector

The simplest morphological edge detectors are the dilation residue and erosion residue operators[L1]. The dilation residue operation is the subtraction of an image from its dilation with a structuring element, while the erosion residue is the subtraction of the erosion of the image from the original image. The difference image is the edge image. As defined in Chapter 3, the dilation of a grayscale image $f(i,j)$ with a grayscale structuring element $e(i,j)$ is

$$D[f,e](i,j) = \max_{l,m} [f(i-l, j-m) + b(l,m)] \tag{5.12}$$

while erosion is

$$E[f,e](i,j) = \min_{l,m} [f(i+l, j+m) - b(l,m)] \tag{5.13}$$

Erosion residue operation is given by

$$G_e[f,e](i,j) = f(i,j) - \min_{l,m} [f(i+l, j+m) - b(l,m)] \tag{5.14}$$

while dilation residue operation is given by

$$G_d[f,e](i,j) = f(i,j) - \max_{l,m} [f(i-l, j-m) + b(l,m)] \tag{5.15}$$

For good edge localization, small structuring elements are used. This makes erosion residue and dilation residue operations sensitive to noise. Larger structuring element can be used to suppress noise, but the edge obtained will be shifted inward or outward with erosion residue or dilation residue operations, respectively. Good edge localization can be achieved with the so-called morphological gradient[G1] (Mgradient) operation which is the subtraction of the erosion of the image from the dilation of the image

$$G[f,e](i,j) = \max_{l,m} [f(i-l, j-m) - b(l,m)] - \min_{p,q} [f(i+p, j+q) + b(p,q)] \tag{5.16}$$

Mgradient will place the center of the edge at the exact boundary of a structure. If constant structuring element is used, i.e. $b(i,j)$ =constant, such as the 8-connected

structuring element

$$\begin{pmatrix} 1 & 1 & 1 \\ 1 & 1 & 1 \\ 1 & 1 & 1 \end{pmatrix}$$

Mgradient can be simplified to

$$G[f,e](i,j) = \max_{l,m} f(i-l, j-m) - \min_{p,q} f(i+p, j+q) \tag{5.17}$$

This is similar to the subtraction of two convolution operations except that maximum and minimum take the place of summation.

Since any structures smaller than the size of the structuring element will be eliminated in the dilation and erosion processes, the Mgradient also has smoothing capability. A comparison of the performance of the Mgradient with that of the Sobel and Canny-Deriche is shown in Figure 5-1. The Sobel, Canny-Deriche and Mgradient operators are applied to a typical double exposure portal image in (a) and the results are shown in (b), (c) and (d) respectively. The edge images have been thresholded with a threshold value at which the closed contour of the treatment field is just found. It can been seen that the Canny-Deriche and the Mgradient are much less sensitive to sharp edges and noise. The Mgradient can give result similar to that given by optimal detectors but is much faster. Even when the IM-1280 board is disabled, the Mgradient takes 3.24 seconds compared to the 17.08 seconds required by the Canny-Deriche for a 256×256 image.

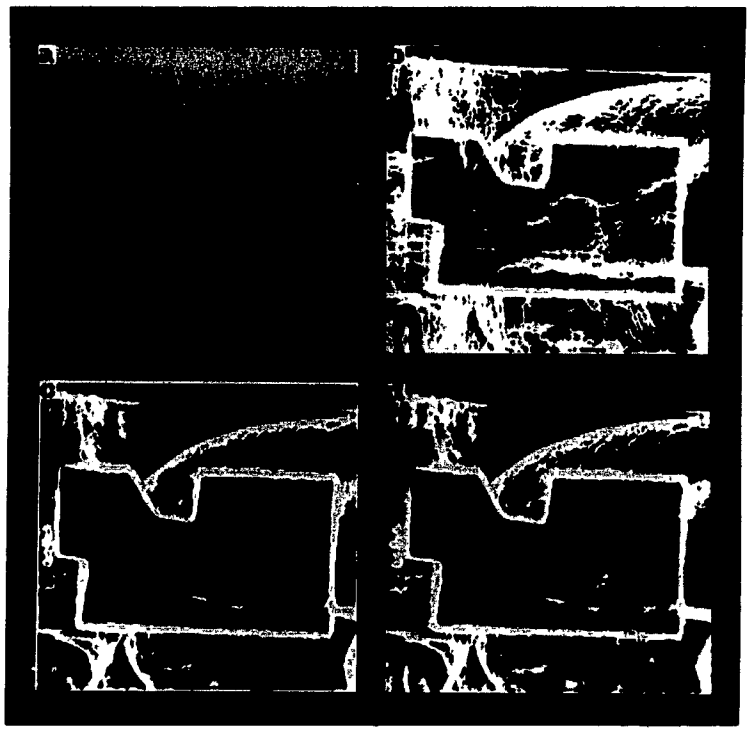

Figure 5-1: Performance of three different edge detectors on a double exposure portal image. The edge images have been thresholded with a threshold value at which the closed contour of the treatment field is just found. (a) original portal image, (b) Sobel, threshold=1, (c) Canny-Deriche, threshold=4, (d) Mgradient, threshold=6.

To test the insensitivity of the Mgradient to noise, three portal films were acquired during one treatment with different amount of radiation to produce different overall noise level, and the resultant detected field edges on the processed images are shown in Figure 5-2. For demonstration purpose only the images obtained by histogram equalization are shown because the contrast of the original portal images is too low to observe any difference in noise levels. The profiles along the middle row of the original image and the enhanced images are plotted. It can be seen that the extracted field border are the same irrespective of noise level.

In the studies, we have preferred the Mgradient detector because of its speed and its low sensitivity to noise. Once the edge has been determined using the Mgradient, we proceed to extract the radiation field to finally automatically segment it from the outer field image.

5.3 Feature extraction

After edge enhancement with Mgradient, a thresholding operation is usually applied to remove noise and unwanted edges. Thresholding is a transform that assigns a single value (usually '1' is used) to all the pixels whose gray value is greater than the threshold and assigns '0' to all the others. Given a grayscale image $I(i,j)$, thresholding by a threshold value T results in a binary image $O(i,j)$,

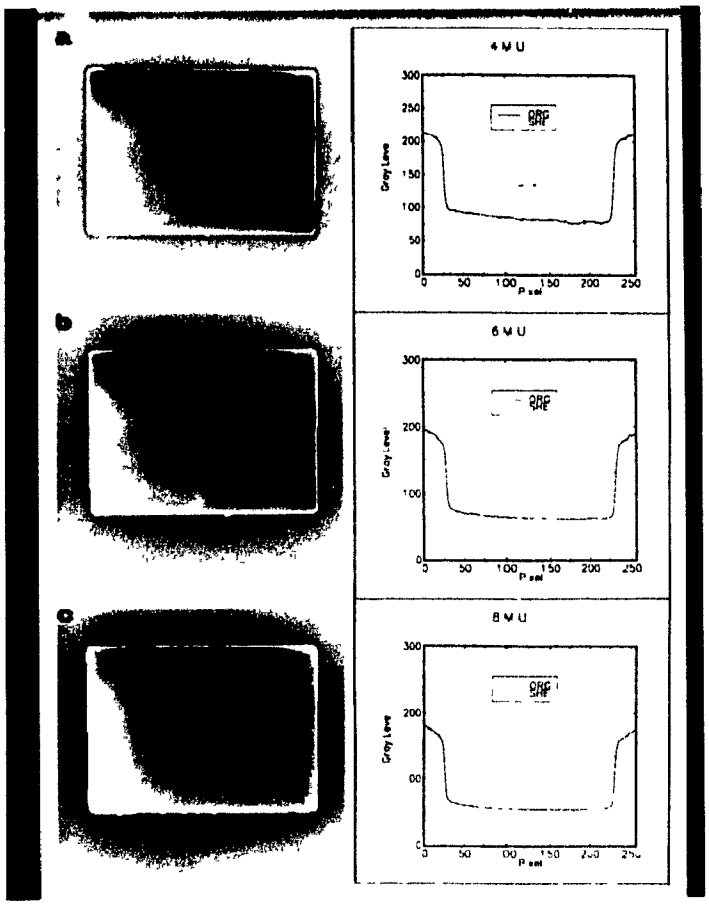

Figure 5-2: Profiles along the middle row of original and enhanced portal images. The portal films are acquired during the same treatment but with different exposure: (a) 4MU, (b) 6MU, (c) 8MU.

$$O(i,j) = \begin{cases} 1, \text{ if } I(i,j) > T \\ 0, \text{ if } I(i,j) < T \end{cases} \tag{5.18}$$

In the case of a double exposure portal image, e.g. Figure 5-1(a), the feature that we want to extract is the closed contour of the treatment field. But the edge intensity along the treatment field contour is not uniform since the treatment field is a transparent shadow on the background anatomy. Therefore, the threshold value is selected as the one at which a closed field contour is formed.

Usually, portal images have a low inherent contrast. If a double exposure portal film is appropriately acquired, i.e. the two exposures are in a reasonable proportion, the treatment field has greater contrast than the anatomy. Therefore, after edge enhancement, the field edge is stronger than the anatomy edges. The closed field contour can be extracted at a threshold value higher than the intensity of the anatomy edges, resulting in a very clean edge.

But on some occasions, the field border may fall on some dark structure, therefore causing some parts of the field edge to be significantly weakened and to become comparable with strong anatomy edges. In order to obtain the closed field contour, the threshold value must be reduced. At the same time, noise and anatomy edges will appear within the binary edge image and may be connected to the field edge, as in Figure 5-1 (d). This poses a big problem to contour connecting techniques because it requires high-level knowledge to differentiate a field edge from anatomy edges. However, if the binary edge image in Figure 5-1 (d) is inverted, closed edges become gaps separating different objects,

and open edges become cracks or holes on objects. The task is changed from extracting the field contour to extracting the object representing the treatment field, and the problem is changed from removing unwanted anatomy edges connected to the field contour to picking up the object corresponding to the treatment field, and closing cracks and filling holes on the object. This process is made much simpler by using morphological techniques than it is by incorporating some form of high-level knowledge into feature extraction algorithms.

After the binary edge image is inverted, it is labeled for analysis in order to isolate the field object. The labeling operation is to differentiate different objects by assigning different gray levels to different objects in a binary image (Figure 5-3).

Objects can then be separated by thresholding at each gray level, and properties like area and perimeter can be calculated such that objects can be analyzed and sorted by their properties.

Image analysis is very time consuming because it involves intensive calculation. We introduced certain models within the analysis to shorten computation time. When a film is digitized, it is always placed at the center of view. Therefore the field always cover the center of a digitized image. Based on this fact, the field object can be extracted with the reconstruction operation (Chapter 4) with a binary marker image which contains a small marker at the image center. For 256×256 images, the marker consists of a disk of radius of 10 pixels. This marker is sufficiently small not to exceed the range of any treatment field in any portal image, and sufficiently large not to miss the field object if

Binary Image

$$\begin{pmatrix} 1 & 1 & 0 & 0 & 0 & 0 & 0 & 0 & 0 & 1 & 1 & 1 & 0 \\ 1 & 1 & 0 & 1 & 1 & 0 & 0 & 0 & 0 & 1 & 1 & 1 & 0 \\ 1 & 0 & 0 & 1 & 1 & 1 & 0 & 0 & 0 & 0 & 0 & 0 & 0 \\ 1 & 0 & 1 & 1 & 1 & 1 & 0 & 0 & 0 & 0 & 0 & 0 & 0 \\ 0 & 0 & 0 & 0 & 1 & 0 & 0 & 0 & 0 & 0 & 1 & 1 & 1 \\ 0 & 0 & 0 & 0 & 0 & 0 & 0 & 0 & 0 & 0 & 0 & 1 & 1 \\ 0 & 0 & 1 & 0 & 0 & 0 & 0 & 0 & 1 & 1 & 0 & 0 & 1 \\ 0 & 0 & 1 & 1 & 1 & 1 & 1 & 1 & 1 & 1 & 0 & 0 & 1 \\ 0 & 0 & 1 & 1 & 1 & 1 & 1 & 1 & 1 & 0 & 0 & 0 & 1 \end{pmatrix}$$

Labelled Image

$$\begin{pmatrix} 1 & 1 & 0 & 0 & 0 & 0 & 0 & 0 & 0 & 2 & 2 & 2 & 0 \\ 1 & 1 & 0 & 3 & 3 & 0 & 0 & 0 & 0 & 2 & 2 & 2 & 0 \\ 1 & 0 & 0 & 3 & 3 & 3 & 0 & 0 & 0 & 0 & 0 & 0 & 0 \\ 1 & 0 & 3 & 3 & 3 & 3 & 0 & 0 & 0 & 0 & 0 & 0 & 0 \\ 0 & 0 & 0 & 0 & 3 & 0 & 0 & 0 & 0 & 0 & 4 & 4 & 4 \\ 0 & 0 & 0 & 0 & 0 & 0 & 0 & 0 & 0 & 0 & 0 & 4 & 4 \\ 0 & 0 & 5 & 0 & 0 & 0 & 0 & 0 & 5 & 5 & 0 & 4 & 4 \\ 0 & 0 & 5 & 5 & 5 & 5 & 5 & 5 & 5 & 5 & 0 & 0 & 4 \\ 0 & 0 & 5 & 5 & 5 & 5 & 5 & 5 & 5 & 0 & 0 & 0 & 4 \end{pmatrix}$$

Figure 5-3: Illustration of the labelling operation

the marker falls on a hole on the field object.

Although the field object picked up by the marker has the same shape with the dark treatment field on the original portal image, its size is smaller because the field edge usually has a width of several pixels. It also has some cracks and holes on it due to the anatomy edges and noise. From our own investigation, we found that applying the closing operation three times is sufficient to close any cracks on any field objects. A hole-filling operation is applied to fill any possible holes on the object. Then the field object is dilated twice to return it to the real size. The flowchart of the mainstream of the segmentation and contrast enhancement is shown in Figure 5-4.

The original portal image is read into memory and the Mgradient operation is applied to it to obtain an edge image. This edge image is thresholded with an optimal threshold value obtained by a program which will be discussed later. After thresholding, this binary edge image is inverted to its complement, and the central object in this image is picked up with the marker image described earlier. This object is then refined to a mask representing the treatment field and the complement of this mask image is the mark representing the surrounding area. The original portal image is segmented into two subimages with these two masks. The two subimages are combined together after applying histogram equalization separately to each of them.

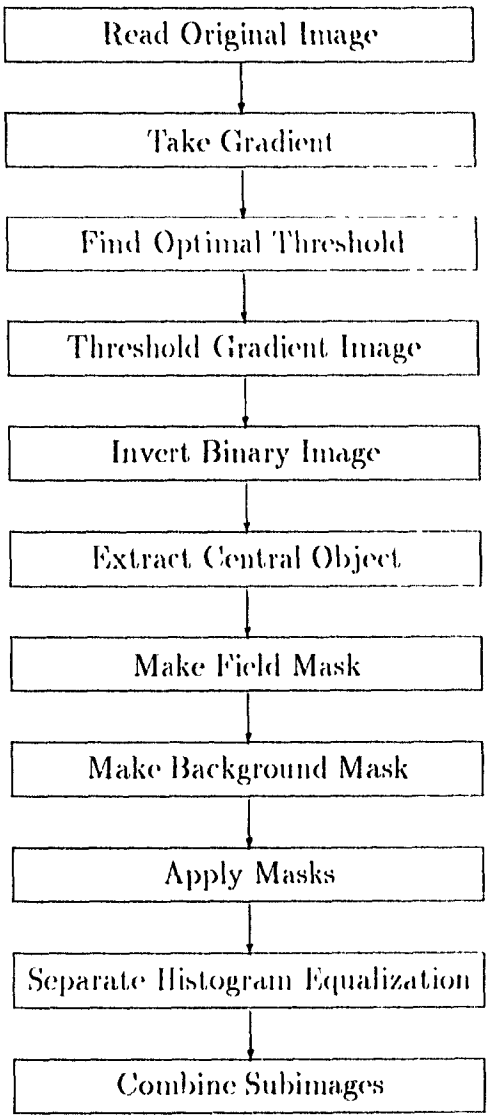

Figure 5-4: Flowchart of the mainstream of the segmentation and contrast enhancement procedure.

5.4 Automation of Segmentation

To be automatic, the algorithm must be capable of adjusting itself to search for an optimal threshold value with which the field extraction procedure mentioned above can proceed. The optimal threshold value could be defined as the highest value at which a closed field contour is just found in the binary image. But, if the field contacts the image border, its contour will be an open curve with both ends on the image border. A better definition has been used, i.e. the optimal threshold value is the highest value at which, in the complement of the binary image, the object corresponding to the treatment field is just separated out from the background. Portal images are acquired for different anatomical sites from different therapy machines and thus have different optimal threshold value.

The searching procedure starts with a high threshold value at which nothing is separated and decrements the threshold value one by one. A predefined area criterion is verified at each threshold value to determined whether to stop the search or not. Due to the complexity of the content of portal images, the procedure has been divided into two stages, each with its own criterion. The first approximation, the flowchart of which is shown in Figure 5-5, is based on a very simple model. Usually, portal images have a very low contrast, and the intensity of the field edge is much greater than that of anatomy edges. While the threshold is being decreased, the field edge will appear first in the binary edge image. This means that in the complement of the binary edge image, a big object of the size of the whole image will break up into two big pieces corresponding to the radiation field and the surrounding area. Therefore, our first approximation is to determine the

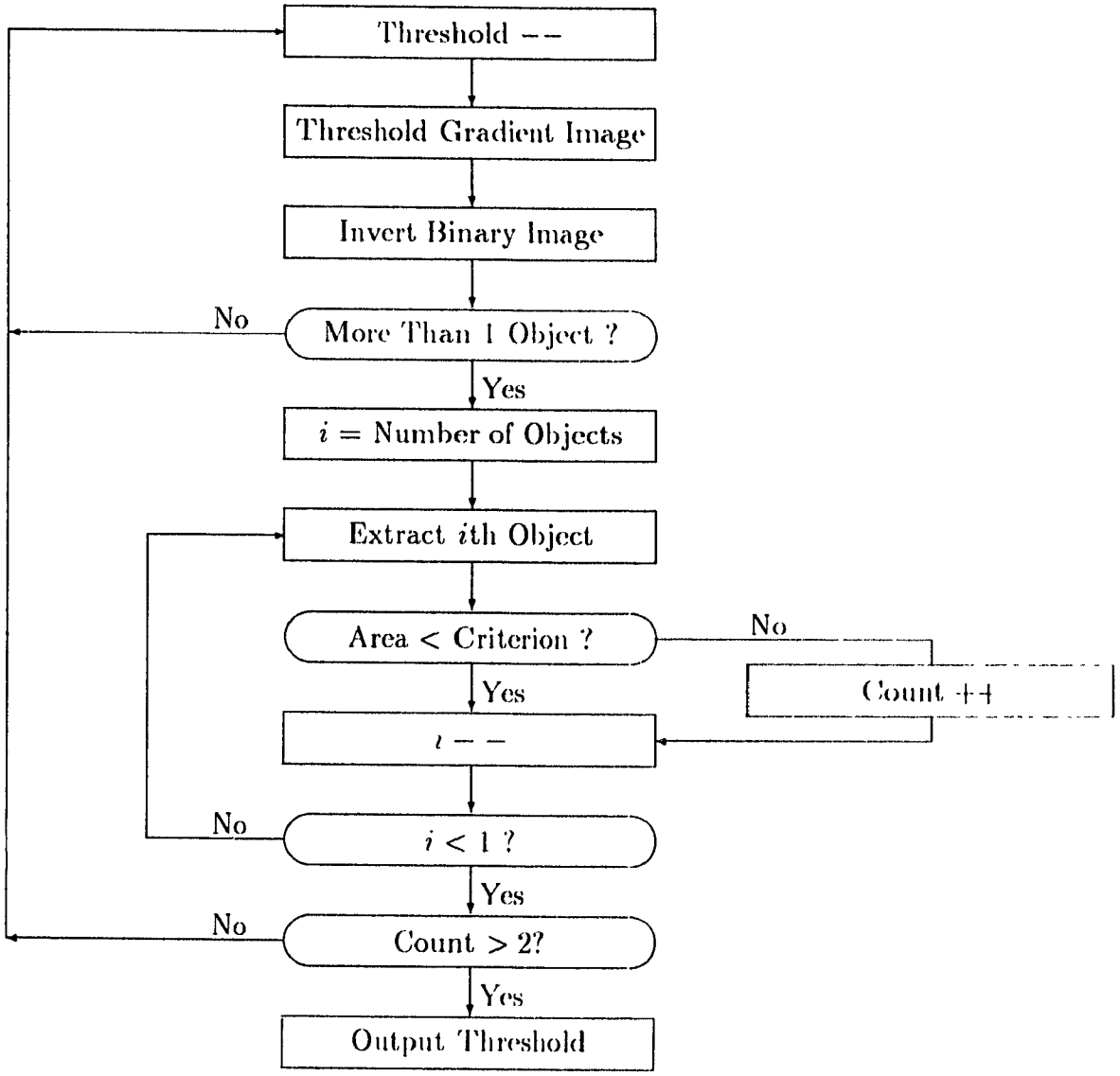

Figure 5-5: Flowchart of the first step of the segmentation procedure.

threshold value at which this just occurs. Starting from the initial threshold value, the program counts the number of separate objects in the complementary of the binary image whose area is larger than a specific criterion. The criterion we chose is $\frac{1}{4}$ of the whole image area. If the number of large objects is smaller than 2, then the threshold value is decremented, and the number of large objects is recounted, and this process continues until two large objects are found.

In some cases, part of the field border may fall on a dark structure (Figure 5-6 a). This part of the field edge will be significantly weakened so that its intensity is probably comparable to that of the strong anatomy edges outside the field. In the complement of the binary image, the background may fall apart into several pieces before the field object comes out completely. Therefore, the area criterion may be met at a threshold value higher than the optimum and, step one is stopped earlier (Figure 5-6 c).

The second stage of the segmentation, whose flowchart is shown in Figure 5-7, is designed to accommodate this difficult situation. After the first approximation, if the field object is still connected to the background, the connection must be weak. The second approximation is to pick up the field object (it may be connected to the background) and verify whether it is compact or not. As described in Chapter 4, the opening operation can break up weak junction which is smaller than the structuring element. Therefore, after the first criterion is met, the program extracts the central object and, opens it four times to verify whether any piece of a significant size can be broken up from this object. At this stage, if any piece can be broken out from the central object, its size

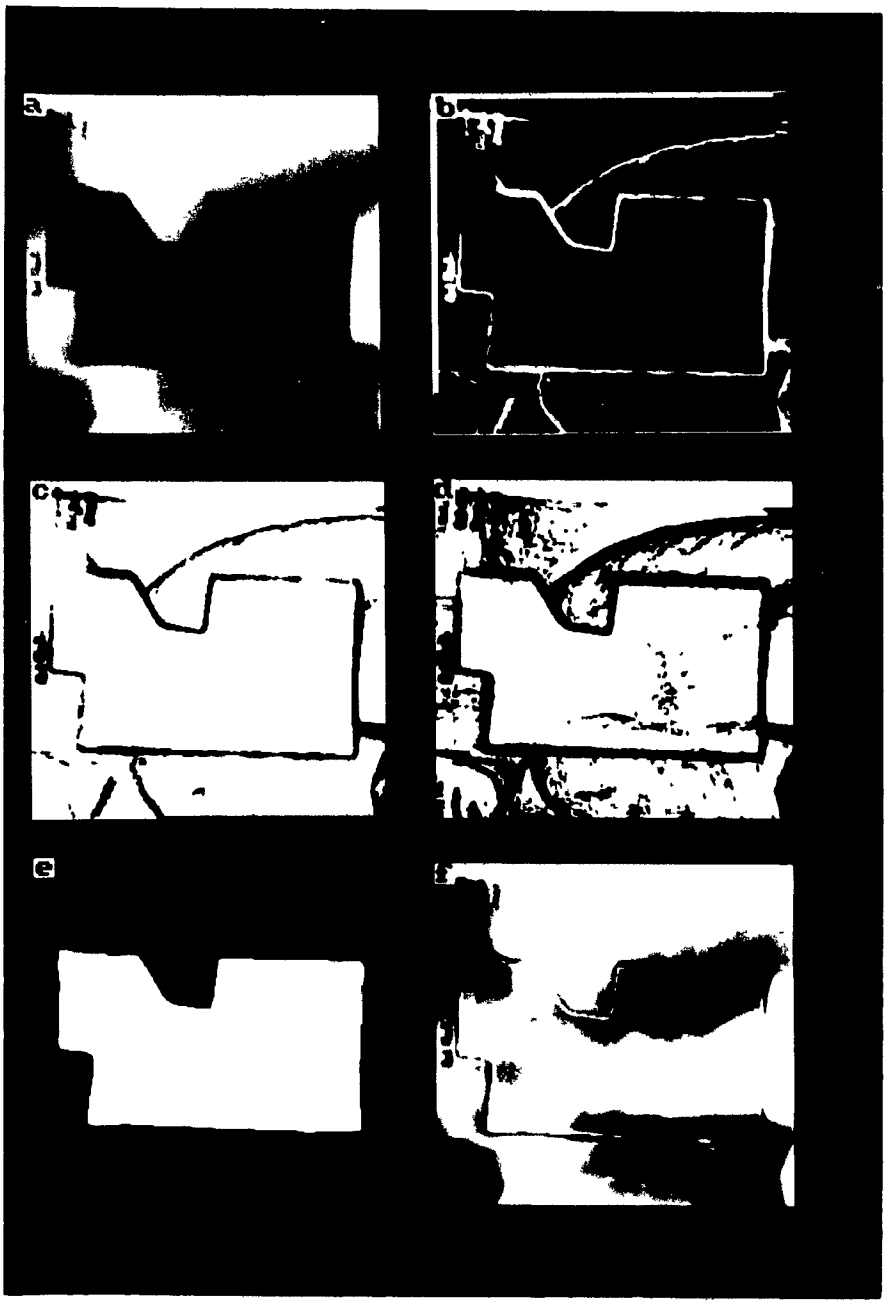

Figure 5-6: Segmentation procedure. (a) original image, (b) binary edge image at the threshold value reached by the first approximation, (c) labeled complement of (b), (d) object image at the optimal threshold value, (e) treatment field mask made from the central object in (d), (f) portal image enhanced with SHE.

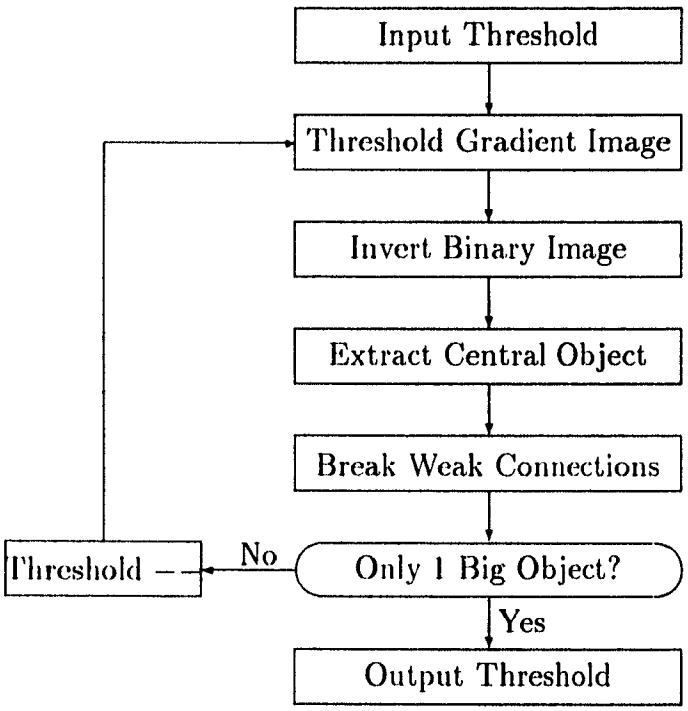

Figure 5-7: Flowchart of the second step of the segmentation procedure.

must be relatively small. The criterion is set as $\frac{1}{65}$ of the whole image area. If, after the opening operation, only one object larger than this criterion is found, then we assume that we have reached the optimum threshold value. Otherwise, the threshold value will be decreased further, and the test will be repeated until the optimal threshold value is reached. Opening with the 8-connected structuring element for 4 times is equivalent to opening with a 9×9 structuring element (Chapter 4). This operation is sufficient to break any inherent junctions on the object because the shape of a prescribed treatment field is sufficiently compact to sustain this operation. Step two does not contradict with step one, since if the optimal threshold value has already been reached by step one alone, step two is automatically satisfied.

This automatic segmentation technique was tested on a large number of portal images acquired from a cobalt unit, 4MV, 6MV and 10MV linacs. The images cover a variety of treatment sites. The algorithm turns out to be accurate, robust and fast. The computation time varies from one image to another because of the dynamic reasoning procedure, but it is less than 15 seconds.

Besides selective histogram equalization, another purpose of automatic segmentation of double images is to accelerate the process of treatment verification. The automatically extracted treatment field mask will be used as the landmark for portal-simulator image correlation which will be discussed in the next chapter.

Chapter 6

Portal Image Registration

As described in Chapter 2, radiation therapy treatments are verified by comparing the portal image with the simulation image. Portal and simulator images have different size, location and orientation on films due to their different geometries in the acquisition. An illustration of films set-up is shown in Figure 6-1.

On the simulator, the cassette is placed right above the image intensifier under the couch, and is positioned as close to the patient as possible to reduce geometric penumbra. But the majority of treatment machines do no presently have built-in on-line portal imagers. Since there is not sufficient room for the cassette in the couch of treatment machines, the cassette is not placed as close to the patient as on the simulator, resulting in portal films being magnified compared to simulator films. Because the fixing of the cassette may be different on the two machines this may result in a tilted portal film. When we digitize the portal and simulator films with the laser scanner, they are inserted into a slot. Therefore the digital images have different size, location and orientation. The purpose of digital imaging is to manipulate the image data so that images of the

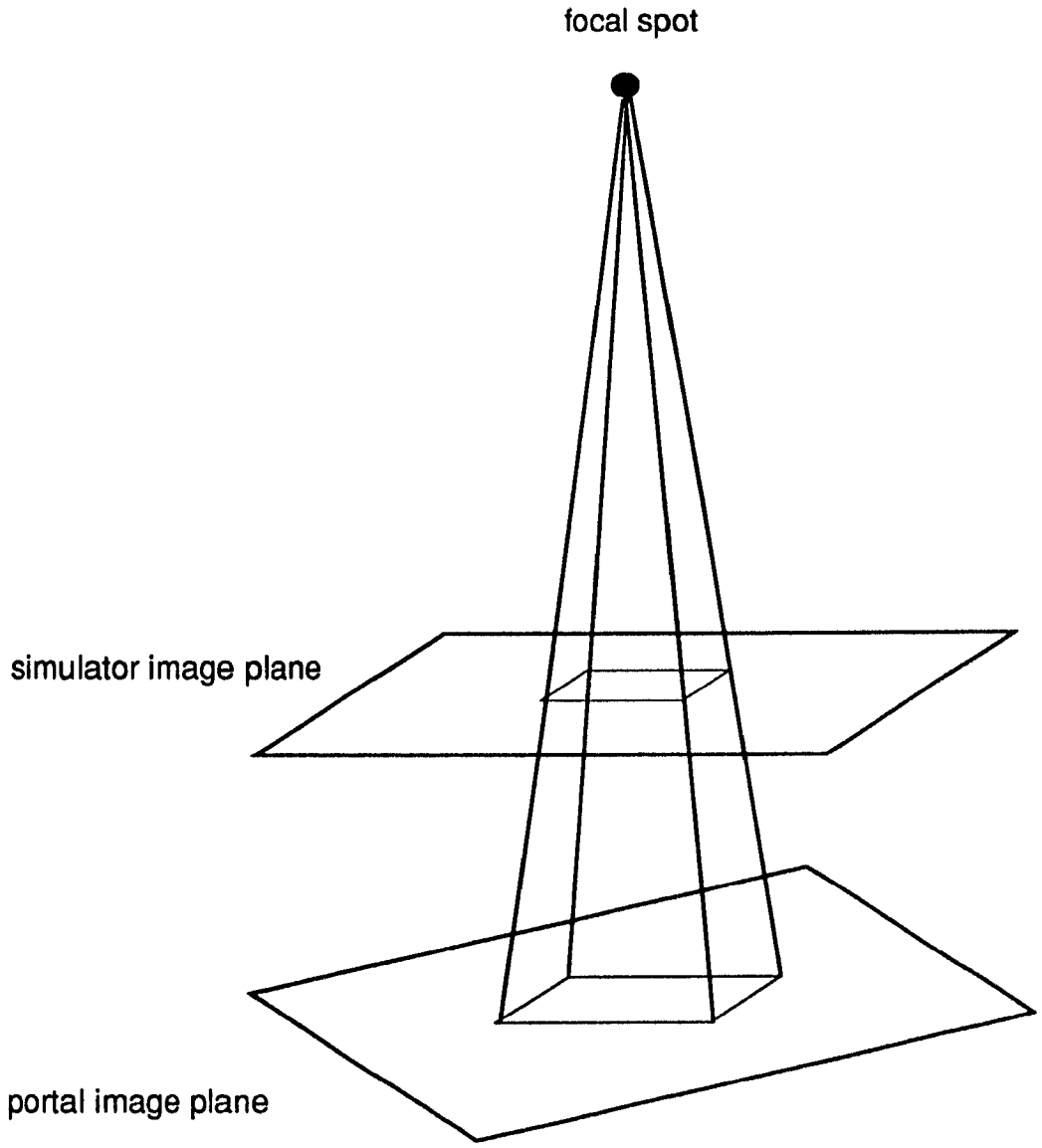

Figure 6-1: Illustration of the geometric relationship between a simulator image and its corresponding portal image.

same object but acquired under different geometry can be transformed into the same geometry for direct comparison. This matching procedure is called image correlation or registration. Correlation of two images is usually achieved by matching some features common to both images. These features correspond to the same object or part of an object.

6.1 Geometric Transformation

A geometric transformation of an image is to change the spatial positioning of pixels in the image. Given an image $I(x,y)$, its spatial positioning in a plane can be achieved with a rotation, a translation, and a size transformation. For an arbitrary pixel located at (x,y), a rotation of an angle θ around a point (x_r,y_r) moves it to (x',y'), where

$$\begin{pmatrix} x' \\ y' \end{pmatrix} = \begin{pmatrix} \cos\theta & -\sin\theta \\ \sin\theta & \cos\theta \end{pmatrix} \begin{pmatrix} x - x_r \\ y - y_r \end{pmatrix} + \begin{pmatrix} x_r \\ y_r \end{pmatrix} \tag{6.1}$$

A translation of the pixel by a vector (x_t,y_t) is simply given by

$$\begin{pmatrix} x' \\ y' \end{pmatrix} = \begin{pmatrix} x \\ y \end{pmatrix} + \begin{pmatrix} x_t \\ y_t \end{pmatrix} \tag{6.2}$$

Scaling is to proportionally change the distance from this pixel to a projection point (x_p,y_p).

$$\begin{pmatrix} x' \\ y' \end{pmatrix} = \begin{pmatrix} m & 0 \\ 0 & m \end{pmatrix} \begin{pmatrix} x - x_p \\ y - y_p \end{pmatrix} + \begin{pmatrix} x_p \\ y_p \end{pmatrix} \tag{6.3}$$

where m is the magnification factor. For portal-simulator image correlation, the transformation parameters are calculated from landmarks.

However, a digital image is represented as a two dimensional array. When the image is rotated or scaled, the new location of a pixel becomes fractionated thus not allowing it to fit within the grid. The image data must be re-sampled to obtain the pixel value at the new location and this is usually achieved by interpolation from the old data. If the new location is simply truncated and the old data is applied to the nearest image grid point, distortion will result in the new image. Interpolation eliminates geometric distortion, but the pixel value obtained by interpolation remains an approximation. The accuracy of interpolation depends on the type of interpolation used. The more accurate the interpolation is, the more time consuming is the calculation. As described in Chapter 2, portal images have low spatial resolution. Under the 256 × 256 mode, we compared the result of nearest neighbor method (no interpolation) with that of the 4-neighbor interpolation, and no difference was seen on the transformed portal images. We thus used the nearest neighbor replication in the transformation of images.

6.2 Landmark Selection

There are two ways to verify a radiation therapy treatment: (a) align the portal and simulator images with respect to some reference anatomy features to observe the shift of the treatment field, or (b) use the treatment field as reference for the alignment to verify any shift in the anatomy. Using anatomical features as landmarks for correlation requires accurate specification of these landmarks on both images, but it is difficult to maintain consistency when choosing the landmarks because the two images are of very different qualities. Since the patient body is not a rigid object, it is also not feasible to place landmarks on or within the patient body that remain stationary with respect to patient anatomy. The radiation field is a pre-specified non-anatomical feature, and as discussed in Chapter 5, we automatically extracted it from the portal image. The same radiation field has already been prescribed on the simulator film and it is very simple to describe the field mask by following the field marked on the simulator film. Therefore, we used the field mask automatically extracted from the portal and the mask described from the prescribed field contour on the simulator image as the control objects for correlation. A binary mask can be considered as a two dimensional uniform rigid object, and two geometrically similar shapes can be correlated by use of their inertia moments[J1][T1][A2].

For a two-dimensional solid uniform object located in the $x - y$ plane, the nth order moment is given by,

$$M^{lm} = \frac{\int (x-a)^l (y-b)^m \, dxdy}{\int dxdy} \tag{6.4}$$

with $a = \frac{\int x dx}{\int dx}$, $b = \frac{\int y dy}{\int dy}$, and $n = l + m$, where l and m are positive integer. Moments up to the second order are sufficient to obtain the geometric relation between two objects (i =1, 2) of geometrically similar shape.

Their relative location can be calculated from the center of mass (a, b), relative orientation can be obtained from the 2nd order inertia moment matrix

$$\begin{pmatrix} M^{20} & M^{11} \\ M^{11} & M^{02} \end{pmatrix} \tag{6.5}$$

and the relative size can be obtained from the eigenvalues of the inertia moment matrix. We used the angle subtended by the greater of the two eigenvectors with the horizontal axis,

$$\theta_i = \arctan\left(\frac{M_i^{02} - M_i^{20} + \sqrt{(M_i^{20} - M_i^{02})^2 - 4(M_i^{11})^2}}{2M_i^{11}}\right) \tag{6.6}$$

to specify the orientation, and used the corresponding eigenvalue,

$$\lambda_i = \frac{1}{2}\left[M_i^{20} + M_i^{02} + \sqrt{(M_i^{20} + M_i^{02})^2 - 4(M_i^{11})^2}\right] \tag{6.7}$$

to specify size. By choosing the center of mass (a, b) as the rotation center and the projection point, the transformation parameters are given by,

$$\begin{pmatrix} x_t \\ y_t \end{pmatrix} = \begin{pmatrix} a_1 - a_2 \\ b_1 - b_2 \end{pmatrix}, \varphi = (\theta_1 - \theta_2), m = \sqrt{\frac{\lambda_1}{\lambda_2}} \tag{6.8}$$

6.3 Results of Registration

The whole procedure of registration is shown in Figure 6-2. The treatment field mask is drawn on the simulator image (a) and is shown in (b). The landmark on the portal image is already automatically extracted (Chapter 5) and is shown in (d). The parameters in the geometric transformation, the translation vector, the rotation angle and the magnification factor, are calculated from the two landmarks, (b) and (d). The enhanced portal image (c) is transformed to the geometry of the simulator image (a) and is shown in (e). The correlated portal (c) and simulator image (a) are overlaid in (f) with the weight 60%-40% for verification. In (f), we can see that the portal and the simulator images are very well aligned but a discrepancy in the shape of the treatment fields is seen at the notch located at the arrow.

Portal-simulator image correlation by using inertia moments of landmarks has been investigated by Bijhold et al[B4].They used the treatment field contour automatically extracted from the portal image and the prescribed field contour which is predrawn on the simulator image as the landmarks for correlation. But the extracted treatment field contour has small fluctuations with respect to the real field border due to noise, and very frequently, discrepancies (could be large) exist between the prescribed field and the treatment field due to the errors in manufacturing the field shaping blocks. A compact

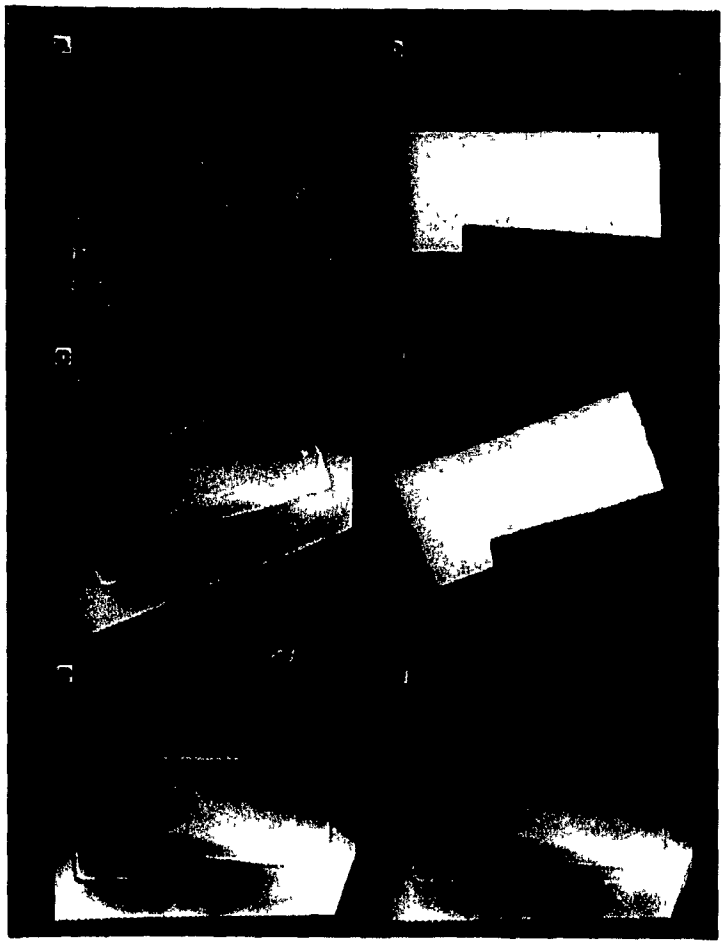

Figure 6-2: Illustration of the registration procedure. (a) simulator image, (b) landmark drawn on the simulator image, (c) enhanced portal image, (d) landmark automatically extracted from the original portal image, (e) portal image after correlation, (f) overlay of the correlated portal and simulator image with a weight of 60% 40%

mask has larger inertia moments than its contour therefore it has stronger resistance to the distortion of the treatment field shape. We compared the results of calculating the inertia moments of the contour with that by calculating the inertia moments of the mask. A double exposure portal film is digitized twice with different film orientation on the lightbox and different camera-to-film distance. The automatically extracted treatment field masks are shown in Figure 6-2 (a) and (b). The two fields are correlated by using the field contours and the field masks as landmarks respectively, as shown in Figure 6-2 (c) and (d). As we had expected, registration with masks appears to offer better performance than registration with contours.

Although using the field masks rather than the field contours results in stronger resistance to field distortion, the inertia moments method will fail if the distortion is too large. According to our observation, large discrepancies in the treatment field shape are so common that they are the factor limiting the effectiveness of this verification procedure. This correlation method was tested on 30 portal-simulator image pairs randomly selected from patient files and 12 of them have very large discrepancies that the algorithm could not give satisfactory correlation. The algorithm's resistance to discrepancy between the prescribed field and treatment field is dependent on the shape of the field because the sensitivity of the inertia moments to a distortion on one geometric shape is different from the same distortion on another. In another word, the magnitude of the discrepency at which the correlation algorithm will fail is different for different geometric shapes and is also dependent on the location of the distortion on the geometric shape. For example,

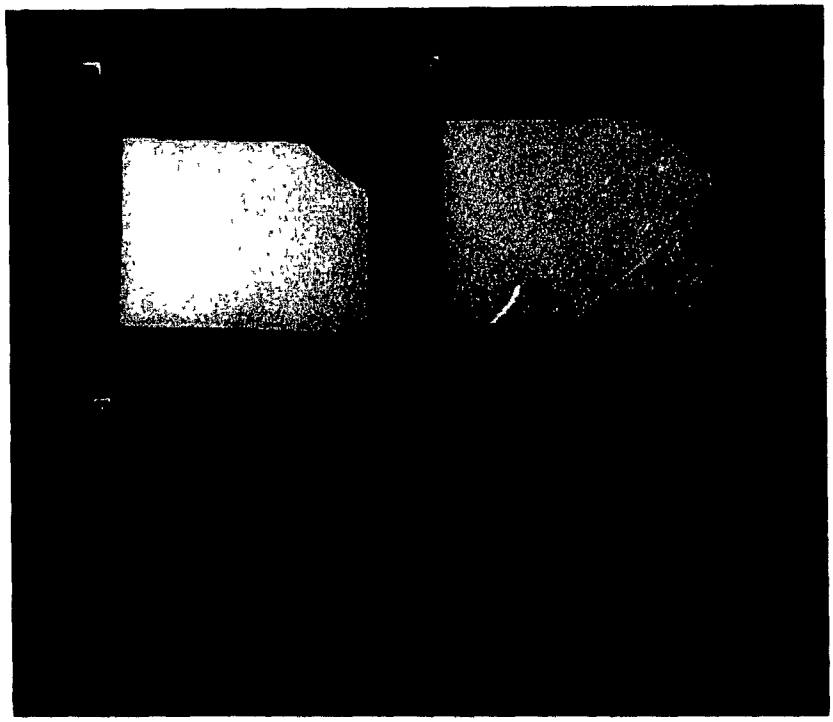

Figure 6-3: Comparison of landmarks. (a) field mask extracted from a double exposure portal image, (b) field mask extracted from another portal image digitized from the same portal film, (c) registration obtained by using the two masks as landmarks, (d) registration obtained by using the two field contours as landmarks.

the influence of distortion on the inertia moments of a square is much larger than that on the inertia moments of a very flat rectangle. The correlation algorithm is not resistant to shape distortions when the treatment field is square. Another limitation of this method is that it does not consider out of plane rotation. But its contribution to the overall error is much smaller than the contribution from field-shaping errors.

Chapter 7

Conclusion

7.1 Summary

A robust algorithm of automatic segmentation and registration of double-exposure portal images has been developed. This algorithm employs mathematical morphology techniques to extract the radiation therapy treatment field out of a double-exposure image and therefore delineate the treatment field and the surrounding area in preparation of: a) the selective histogram (or adaptive histogram) equalization technique used for contrast enhancement of the portal image, b) the landmark for portal-simulator image correlation. Basic principles and operations of mathematical morphology are introduced and specific techniques employed in this algorithm are explained. A fundamental issue in computer vision and pattern recognition, edge detection, is discussed in detail. The performance of three edge detectors, the Sobel, the Canny-Deriche and the morphological gradient on portal images is compared, and the effectiveness of the knowledge-based approach is justified.

Classical geometric moments up to the second-order are used for portal-simulator image correlation. A non-inherent feature but common to the corresponding portal and simulator image is selected as landmark for registration in order to be objective in the treatment verification procedure.

7.2 Algorithm Evaluation

7.2.1 Segmentation

The segmentation technique has been tested on a large number of double exposure portal image taken on a Cobalt unit, 4MV, 6MV and 10MV linear accelerators, and the images cover a large variation of treatment site. The segmentation algorithm has been proven accurate, robust and fast. The calculation time depends on the content of the portal image but is less than 15 seconds. These advantages originates from the following factors.

Morphology gradient

Local gradient operators are designed to give good localization of local edges but they are also sensitive to noise because of their small kernel size and sharp shape. Global edge detectors are based on smoothing filters to suppress noise and weak edges. The filters usually have finite extent therefore they require convolution with a large size kernel. Computation time can be shortened by using recursive methods where the number of calculations is independent of the width of the filter. Deriche has proven that according to the Canny criteria, the Canny-Deriche operator performs better than the first derivative

of the Gaussian in noise suppression and in edge localization. Another advantage is that it requires less number of calculations, resulting in substantial saving of computation time. Calculation time can be saved further by using the morphological gradient. The performance of the Sobel, the Canny-Deriche and the Mgradient operators on portal images has been compared in Chapter 5. Mgradient gives similar results to the Canny-Deriche detector but is much faster.

Multiple criteria and dynamic reasoning

Morphological techniques have been used by Crooks et al[C3][C4] for automatic segmentation of double exposure portal films. But the segmentation was based on a single static criterion, a predefined threshold value. However, to accommodate a much larger variation of portal image types, the algorithm presented here uses a dynamic approach to search for the optimal threshold image for each individual portal image. Because of this, it is capable of easily accommodating very difficult situations, such as the example shown in Figure 5-1 (a). The two predefined criteria are not sensitive to the variation in the content of portal images.

7.2.2 Registration

Image correlation by using inertia moments of landmarks is based on the condition that the landmarks are geometrically similar objects. Theoretically, the treatment field has the same shape with the prescribed field because the blocks used to shape the treatment field

are manufactured according to the field marks prescribed on the simulator film. But very frequently, discrepancy occurs. Although the field mask has stronger resistance to field distortion than the field contour, the inertia moments method will fail if the discrepancy in field shapes between the two images is too large. Nonetheless, unsuccessful correlation is an indication that the treatment field does not correspond to the field prescribed on the simulator image. The verification process has at least, indicated the existence of a discrepancy. If more care is taken in the manufacturing of the field shaping blocks, the success rate of this method will increase significantly. In the case of fractionated treatment, if the treatment is verified by comparing the portal with another portal which has been verified, this method is much more effective since the field shaping blocks are fixed on the tray through out the whole treatment process.

7.3 Future Work

Up to now, the factor that limits the success rate of the segmentation algorithm is improper exposure of the portal film. The ratio of the amount of the two exposures are not reasonable on a double exposure portal film, e.g. the open field exposure is large that the anatomy contrast is comparable with that of the field contrast. Even the eye cannot differentiate the treatment field and the anatomy. This makes the extraction of the treatment field impossible. Therefore, image acquisition should be integrated into the whole procedure. As a matter of fact, this project is also an investigation of on-line treatment set-up and monitoring. With an on-line portal imager, optimization in image

acquisition can be expected so that improved performance of the segmentation can be achieved.

Calculation time is an important issue for on-line portal imaging systems. In the mean time, the algorithm is implemented in a relatively high level, i.e. using standard image processing modules in the Visilog library. Speed can be improved if the algorithm is implemented by using the low level drivers of the image processing board directly. If an interface between the IM 1280 board and the on-line imager is built, the algorithm can be modified to a live-processing mode. Although the algorithm is already very robust, its success rate can still be improved by incorporating high level knowledges. Ultimately, a database can be introduced to build an expert system.

The registration algorithm is developed only for the inspection of treatment field shift. But it has been observed that a large percent of treatment fields do not match the prescribed fields. Sometimes the discrepancy is so large that it can be noticed visually. If large distortion of the treatment field exists, it is no longer reasonable to use the field mask as the reference of registration. Therefore, either more care has to be taken in the manufacturing of the field shaping blocks, or some other feature, such as anatomical landmarks, can be used as reference eventhough they may be difficult to specify

Since fast speed has been pursued during the development of the algorithm, the program is not user friendly. Graphics tools are needed to aid the verification procedure because after correlation, it still requires the operator to look at the images to determine whether there is any shift of the anatomy. With such tools, it would be very easy to

quantify the verification. For example, a ruler function can be provided so that a radiation oncologist can use a mouse to specify the shift of an anatomical feature on the image overlay to calculate the size of the shift. Or, features can be specified on the enhanced portal and on the simulator image from which the shift can be automatically calculated. With a user friendly interface, the program can be refined into a clinically operational software for on-line and off-line treatment verification.

Bibliography

[A1] American Association of Physicists in Medicine (AAPM), Report No. 24, "Radiotherapy Portal Image Quality", *Report of AAPM Task Group No. 28*, AAPM, New York, 1987.

[A2] Yaser S. Abu-Mostafa, and Demetri Psaltis, "Image Normalization by Complex Moments", *IEEE Transactions on Pattern Analysis and Machine Intelligence*, vol. **PAMI-7**, pp. 46-55, 1985.

[B1] D. H. Ballard and C. M. Brown, *Computer Vision*, Prentice-Hall, New Jersy (1982).

[B2] J. Balter, C. A. Pelizzari, and G. T. Y. Chen, "Correlation of Projection Radiographs in Radiation Therapy Using Open Curve Segments and Points", *Medical Physics*, Vol. **19,** pp. 329-334, 1992.

[B3] J. Bijhold, K. G. A. Gilhuijs, M. van Herk, and H. Meertens, "Radiation field edge detection in portal images," *Physics in Medicine and Biology*, vol. **36**, pp. 1705-1710, 1991.

[B4] J. Bijhold, K. G. A. Gilhuijs, and M. van Herk, "Automatic Verification of Radiation Field Shape Using Digital Portal Images," *Medical Physics*, Vol. **19**, pp. 1007-1014, 1992.

[B5] A. L. Boyer, L. Antonuk, A. Fenster, M. van Herk, H. Meertens, P. Munro, L. E. Reinstein, J. Wong, "A Review of Electronic Portal Imaging Devices", *Medical Physics* vol. **19**, pp. 1-16, 1992.

[C1] J. F. Canny, "A Computational Approach to Edge Detection", *IEEE Transactions on Pattern Analysis and Machine Intelligence*, vol. **PAMI-8**, pp. 679-698, 1986.

[C2] I. Crooks and B. G. Fallone, "PC-based Selective Histogram Equalization for Contrast Enhancement of Portal films," *Medical Physics* (abstract), vol. **18**, pp. 618, 1991.

[C3] I. Crooks and B. G. Fallone, "Automatic Segmentation of Portal Images for Selective Histogram Equalization," *Medical Physics* (abstract), vol. **19**, pp. 822, 1992.

[C4] I. Crooks and B. G. Fallone, "Contrast Enhancement of Portal Images by Selective Histogram Equalization", *Medical Physics*, vol. **20**, pp. 199-204, 1993.

[D1] L. S. Davis, "A Survey of Edge Detection Techiniques", *Computer Graphics and Image Processing*, vol. 4, pp. 248-270, 1975.

[D2] R. Deriche, "Using a Canny's Criteria to Derive a Recursively Implemented Optimal Edge Detector", *International Journal of Computer Vision*, vol. **1**, pp. 167-187, 1987.

[D3] E. R. Dougherty and C. R. Giardina, *Matrix Structured Image Processing*, Prentice-Hall, New Jersey, 1987.

[G1] C. R. Giardina and E. R. Dougherty, *Morphological Methods in Image and Signal Processing*, Prentice-Hall, New Jersey, 1988.

[H1] S. R. Sternberg, "Grayscale morphology", *Computer Vision, Graphics and image Processing*,Vol **35**, pp. 333-355, 1986.

[J1] Anil K. Jain, *Fundamentals of Digital image Processing*, Prentice-Hall, Englewood Cliffs, New Jersy, 1989.

[J2] H. E. Johns and J. R. Cunningham, *The Physics of Radiology, 4th Edition*,Charles C. Thomas, Springfield, Illinois, 1983.

[L1] J. S. J. Lee, R. M. Haralick and L. G. Shapiro, "Morphological edge detection", *Proceedings of 8th International Conference on Pattern Recognition*, pp. 369-373, 1986.

[L2] K. W. Leszczynski, S. Shalev, and N. S. Cosby, "The Enhancement of Radiotherapy Verification Images by an Automated Edge Detection Technique," *Medical Physics*, vol. **19**, pp. 611-621, 1992.

[M1] D. Marr and E. Hildreth, "Theory of edge detection", *Proceedings of Royal Sociaty of London*, vol **B 207**, pp. 187-217, 1980.

[M2] G. Matheron, *Random Sets and Integral Geometry*, John Wiley & Sons, New York, 1975

[M3] H. Meertens, J. Bijhold, and J Strackee, "A Method for the Measurement of Field Placement Errors in Digital Portal Images", *Physics in Medicine and Biology*, Vol **35**, pp. 299-323, 1990.

[N1] *Visilog Manual*, Noesis Vision Inc. France.

[P1] W. Pratt, *Digital Image Processing*, John Wiley & Sons, New York, 1978.

[P2] J. M. S. Prewitt, "Object enhancement and extraction", in *Picture Processing and Psychopictorics*, B. S. Lipkin and A. Rosenfeld (Eds.), Academic Press, New York (1970).

[R1] L. G. Roberts, "Machine perception of three dimensional solids", in *Optical and Electro-optical Information Processing*, MIT Press, Cambridge, Massachusetts (1965).

[S1] J. Serra, *Image Analysis and Mathematical Morphology*, Academic Press, London, 1982.

[S2] R. M. Haralick, S. R. Sternberg and X. Zhuang, "Image analysis using mathematical morphology", *IEEE Transactions on Pattern Analysis and Machine Intelligence*, Vol. **9**, pp. 532-550, 1987.

[T1] Cho-Huak Teh, and Roland T. Chin, "On Image Analysis by the Methods of Moments", *IEEE Transactions on Pattern Analysis and Machine Intelligence*, vol. **PAMI-10**, pp. 496-512, 1988.

[T2] M. M. Ter-Pogossian, *The Physical Aspects of Diagnostic Radiology*, Harper & Row, New York, 1967.